

Characterizing Quantum Dots in Semiconductor Hetero-structures

Bachelor's Thesis Project I

Devashish Shah

Roll no: 200260015

Supervisor

Prof. Suddhasatta Mahapatra



Engineering Physics,
Indian Institute of Technology, Bombay

Acknowledgements

I would like to thank Professor Sudhsatta Mahapatra for his continual support and guidance, academic and otherwise. I am also grateful for the insightful discussions and key lessons in low-temperature measurements I learned from interactions with Professor Sudhasatta Mahapatra and Professor Kantiay Dasgupta.

I would also like to thank the graduate students I worked with. Mr. Sounak Samatha, for the guidance and help with instrumentation and measurements. Mr. Siddarth Rastogi and Ms. Varsha Jangir for sharing their knowledge of nano-fabrication and for their persistent effort toward the fabrication of the devices measured. Mr. Bikash C. Barik for the regular guidance with details regarding the quantum transport experimental setup.

Abstract

The quest for the experimental realization of Quantum Processors for computation has grown to be a vast field of research in recent years, with the search for an optimal platform for scalable qubits having become an active area of research in the field. Semiconductor spin qubits and superconducting qubits are at the forefront of research in experimental quantum computing, with keen interest from academia and industry alike. Electron (or Hole) spins in an external magnetic field are natural candidates for a quantum two-level system that can be used as a qubit. With coherent control, spin-readout, and multi-qubit gates having been demonstrated, among other aspects, they are strong candidates for achieving scalable quantum processors.

This thesis focuses on measurements involved in characterizing gate-controlled quantum dots in semiconductor heterostructures. Particular attention is paid to the analysis of measured data and instrumentation involved in setting up low-temperature measurements. All measurements were done at the Silicon Quantum Computing Lab at IIT Bombay.

Contents

1 Semiconductor Spin Qubits	5
1.1 Introduction	5
1.2 DiVincenzo criteria	6
1.3 Loss DiVincenzo Spin Qubit	6
2 Device Structure	13
2.1 AlGaAs and SiGe	13
2.2 Fabrication	15
3 Characterizing the Quantum Well	18
3.1 GaAs AlGaAs Hall Bar	19
3.2 Si SiGe Hall Bar	25
4 Transport Through Quantum Dots	29
4.1 The Constant Interaction Model	29
4.2 Coulomb Spectroscopy	31
4.3 Tunnel Barriers and Electron Temperature	33
5 T₁ and T₂ Measurement	36
5.1 Charge Sensing	37
5.2 Elzerman Spin readout (ERO)	38
5.3 T ₁ Measurement using ERO	39
6 Quantum Transport Measurement Setup	40
6.1 Dilution Refrigerator	40
6.2 Reflectometry	44
7 Future Work and Summary	47

A Appendix	48
A.1 Quantum Hall Effect	48

Chapter 1

Semiconductor Spin Qubits

1.1 Introduction

The intrinsic spin degree of freedom of an electron is a purely quantum mechanical property and is a natural candidate for making a quantum bit: qubit, with spin-up $|\uparrow\rangle$ and spin-down $|\downarrow\rangle$ forming the two orthogonal states constituting the qubit. Harnessing these spin states for applications in quantum information and computing is an aspect this thesis focuses on. Although the field of experimental quantum computing is relatively young, magnetic properties arising from this intrinsic spin magnetic moment of Fermions have been exploited extensively, with memory devices, magnetic read leads, and medical imaging (MRI) being a few examples. All of these applications rely on the manipulation and measurement of the net magnetization vector of a material using an external drive. Despite the intrinsic spin of an electron (or nuclear spin) being a purely quantum mechanical property, in nearly all practical cases where one works with a large ensemble of spins, the quantum state decoheres so quickly that no quantum effects can be observed. One effectively takes into consideration the net magnetization vector, which behaves like a classical magnetic moment.

To be able to observe and manipulate quantum effects of the spin magnetic moment, one needs a system where a few spins can be isolated at very low temperatures. Electron spins confined in *gate-defined semiconductor quantum dots*, cooled down to cryogenic temperatures, are such a system. To understand why these are good qubit candidates, a natural starting point is revisiting the DiVincenzo criteria.

1.2 DiVincenzo criteria

In 1998, Daniel Loss and Daniel P. DiVincenzo [11] proposed an implementation of universal one and two-qubit quantum gates for quantum computation using spin states of coupled single-electron quantum dots, followed by a work by Daniel P. DiVincenzo in 2000 [3], which laid down the preliminary requirements for realizing functional qubits for quantum computation. The *DiVincenzo criteria* can be summarized as follows:

1. **Scalable well characterized qubits:** The physical parameters of the qubit are accurately known, namely its internal Hamiltonian and couplings or interactions with other qubits and the environment. Equivalently, one should be able to fabricate a well-defined two-level quantum system in a reliable, reproducible manner,
2. **High fidelity initialization:** Initializing a qubit (or a qubit array) to a well-defined initial state must be possible at times much shorter than the decoherence time T_2 .
3. **Decoherence times much longer than the gate operation time:** The quantum system must remain coherent for times much longer than the duration of execution of logic gates to allow fault-tolerant computation.
4. **Universal set of quantum gates:** It should be possible to execute a universal set of quantum logic gates, for instance, the single-qubit Pauli gates, and the two-qubit CNOT is one set.
5. **Qubit-specific measurement capability:** Post operation, it should be possible to read out the final state of the qubit array with acceptable fidelity.

1.3 Loss DiVincenzo Spin Qubit

Having laid out the criteria that a physical realization of a qubit must meet, it is fruitful to first start with a completely mathematical description of a DiVincenzo spin qubit and how one would drive such a two-level system (criterion 4 in sec 1.2)¹.

¹This section describes an idealized system without getting into complications of state preparation, readout, etc. It is a summary of the physics that lies behind the realization of a universal set of gates for a DiVincenzo qubit [21].

We start with single electron spins $\vec{S}_i = \frac{\hbar}{2}\vec{\sigma}_i$ mapped to Pauli matrices in an external magnetic field. The Zeeman split spin states form the quantum two-level system. The Hamiltonian describing several such spin qubits coupled to one another is:

$$\hat{H}(t) = \frac{1}{4} \sum_{(i,j)} J_{ij}(t) \vec{\sigma}_j \cdot \vec{\sigma}_i - \frac{1}{2} \sum_i g_i \mu_B (\vec{B}_i^0 + \vec{B}_i(t)) \cdot \vec{\sigma}_i \quad (1.1)$$

The first term is the Heisenberg Hamiltonian with J_{ij} being the exchange coupling between the i^{th} and the j^{th} spin and the second term is the Zeeman term ($-\vec{\mu} \cdot \vec{B}_{tot}$). Time-dependent fields $\vec{B}_i(t)$ and site-based g -factor modulation allow for qubit operations in the presence of a DC Zeeman field. The static fields \vec{B}_i^0 may also be made to vary slightly for each site. The unperturbed Hamiltonian for a single spin in a DC magnetic field $\vec{B} = B_0 \hat{z}$ in the σ_z basis is:

$$\hat{H}_0 = \frac{\hbar\omega_L}{2} \begin{bmatrix} -1 & 0 \\ 0 & 1 \end{bmatrix} \quad (1.2)$$

Here, $\omega_L = geB_0/2m^*$ is the Larmor frequency. The eigenstates of the Hamiltonian are $|0\rangle = [1 \ 0]^T$ and $|1\rangle = [0 \ 1]^T$, with eigenvalues $-\hbar\omega_L/2$ and $\hbar\omega_L/2$ respectively. These are the logic LOW and logic HIGH states of the quantum bit. In contrast to a classical bit, any general state vector can be a superposition of these two eigenstates:

$$\psi = \alpha |0\rangle + \beta |1\rangle = \begin{bmatrix} \alpha \\ \beta \end{bmatrix} \quad (1.3)$$

Here $\alpha, \beta \in \mathbb{C}$, and $|\alpha|^2 + |\beta|^2 = 1$, with $|\alpha|^2$ and $|\beta|^2$ being the probability of finding the system in state $|0\rangle$ and $|1\rangle$ respectively. A very convenient visualization of this 2D space spanned by the eigenvectors is the Bloch sphere representation², where $\alpha = \cos(\frac{\theta}{2})$ and $\beta = e^{i\phi} \sin(\frac{\theta}{2})$. An arbitrary state vector in the 2D Hilbert space can then be mapped to a unique point on a unit sphere ($\psi = \psi(\theta, \phi)$) called the Bloch sphere.

$$\psi = \cos\left(\frac{\theta}{2}\right) |0\rangle + e^{i\phi} \sin\left(\frac{\theta}{2}\right) |1\rangle = \begin{bmatrix} \cos\left(\frac{\theta}{2}\right) \\ e^{i\phi} \sin\left(\frac{\theta}{2}\right) \end{bmatrix} \quad (1.4)$$

²Global phases of the state $|\psi\rangle$ have no physical implication and can be ignored; thus, here α is taken to be real without loss of generality.

Unitary time evolution of the state $|\psi\rangle$ can be seen as a precession about the z-axis on the Bloch sphere (fig 1.1 (a)):

$$\begin{aligned}\psi(t) &= \cos\left(\frac{\theta}{2}\right)|0(t)\rangle + e^{i\phi}\sin\left(\frac{\theta}{2}\right)|1(t)\rangle \\ &= e^{i\omega_c t/2} \left[\cos\left(\frac{\theta}{2}\right)|0\rangle + e^{i(\phi-\omega_c t)}\sin\left(\frac{\theta}{2}\right)|1\rangle \right]\end{aligned}\quad (1.5)$$

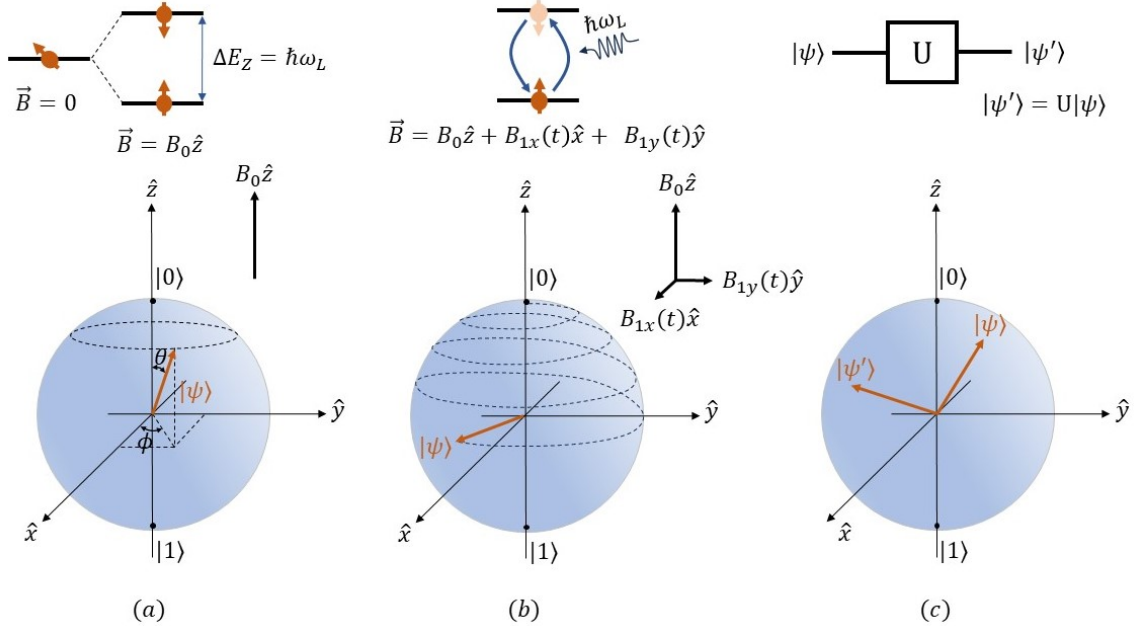


Figure 1.1: (a) Bloch sphere representation of an arbitrary qubit state. (b) Qubit operation using a resonant AC field. (c) A generic unitary operation on a Bloch sphere.

Any unitary operation $|\psi'\rangle = U|\psi\rangle$, where $U^\dagger U = \mathbb{I}_{2\times 2}$, i.e., any single qubit gate, can be shown to correspond to a rotation on the Bloch sphere (section 1.3.1. [14]). For the Hamiltonian in equation (1.2), these unitary operations can be achieved by applying a small oscillating magnetic field perpendicular to the quantization axis.

Driving a Single Qubit

Transitions between the two-qubit levels can be driven using a time-dependent perturbative field $\vec{B}_1(t)$, with $B_1 \ll B_0$. Say, we start with the state $|0\rangle$ at $t = 0$ and apply a rotating field $\vec{B}_1(t) = B_1 \cos(\omega t)\sigma_x + B_1 \sin(\omega t)\sigma_y$. The state at any time t is

then given by $|\psi(t)\rangle = c_0(t)|0\rangle + c_1(t)|1\rangle$. The Hamiltonian of this system is:

$$\begin{aligned}\hat{H} &= \hat{H}_0 + \hat{H}' = -\frac{1}{2}g\mu_B(B_0\sigma_z + B_1\cos(\omega t)\sigma_x + B_1\sin(\omega t)\sigma_y) \\ &= -\frac{E_L}{2}|0\rangle\langle 0| + \frac{E_L}{2}|1\rangle\langle 1| - V e^{-i\omega t}|0\rangle\langle 1| - V e^{i\omega t}|1\rangle\langle 0|\end{aligned}\quad (1.6)$$

$E_L = \hbar\omega_L$ and $V = g\mu_B B_1/2$. This is one of the few exactly solvable problems in time-dependent perturbation theory ($i\hbar \dot{c}_m(t) = \sum_n c_m(t) \langle m | H' | n \rangle e^{i\omega_{mn}t}$). The solution to this problem is:

$$|c_1(t)|^2 = \frac{V^2/\hbar^2}{V^2/\hbar^2 + (\omega - \omega_L)^2/4} \sin^2 \left\{ \left[\frac{V^2}{\hbar^2} + \frac{(\omega - \omega_L)^2}{4} \right]^{1/2} t \right\} \quad (1.7)$$

$$|c_0(t)|^2 = 1 - |c_1(t)|^2 \quad (1.8)$$

The probability of finding the higher energy state oscillates with frequency two times that of $\Omega = \left[\frac{V^2}{\hbar^2} + \frac{(\omega - \omega_L)^2}{4} \right]^{1/2}$. Equation (1.7) is the Rabi formula and Ω is the Rabi frequency. When the frequency of the oscillating pulse is resonant with the Zeeman splitting, i.e., $\omega = \omega_L$, the oscillation amplitude is maximum and equals one.

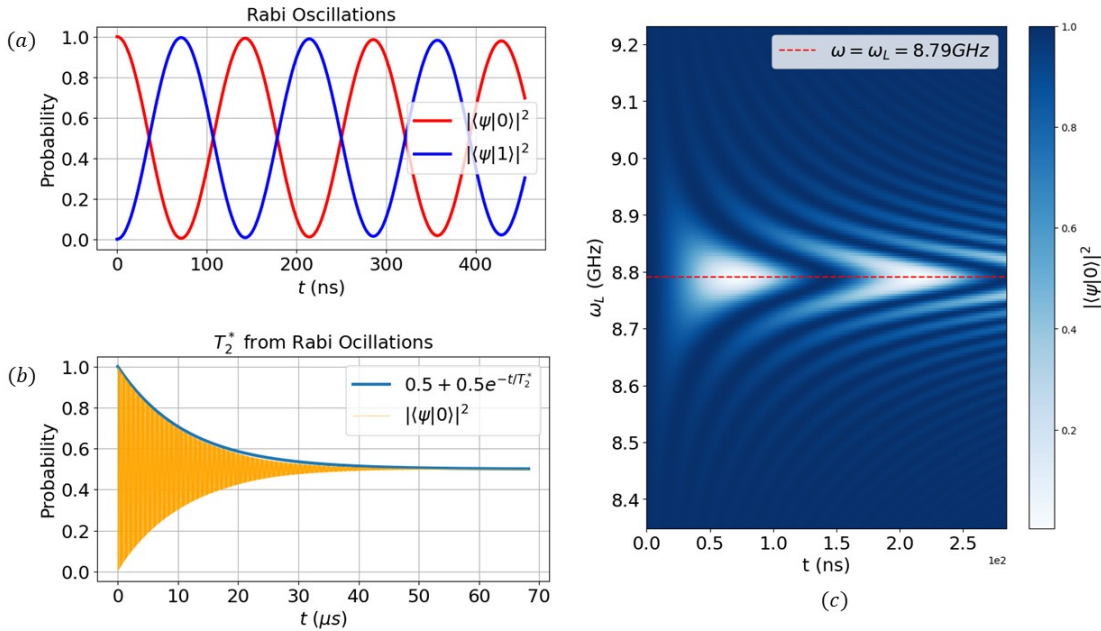


Figure 1.2: Qutip simulations: (a) Rabi oscillations between states $|0\rangle$ and $|1\rangle$. (b) Decaying Rabi amplitude due to decoherence gives a measure of the decoherence time T_2^* . (c) A drive frequency sweep which is used (experimentally) to obtain the Larmor frequency of the qubit. Driving off-resonance gives negligible oscillation amplitude.

A more complete description of the system is one that includes dissipative interactions of the spin qubit with the environment. The total state of the qubit + environment (density matrix ρ_{tot}) then evolves according to the von Neumann equation $\dot{\rho}_{tot}(t) = -\frac{i}{\hbar}[\hat{H}_{tot}, \rho_{tot}(t)]$. The state of the system $\rho = Tr_{env}(\rho_{tot})$ obtained by tracing out the environment evolves in accordance to the Lindblad master equation:

$$\dot{\rho} = \mathcal{L}(\rho) = -\frac{i}{\hbar}[\hat{H}(t), \rho(t)] + \sum_n \left[L_n \rho L_n^\dagger - \frac{1}{2} L_n^\dagger L_n \rho - \frac{1}{2} L_n L_n^\dagger \rho \right] \quad (1.9)$$

The first term is the unitary evolution generated by the Hamiltonian. Whereas the second term encompasses interactions with the environment. The operators L_n are called Lindblad operators or quantum jump operators [15]. Each $L_n \rho L_n^\dagger$ term induces one of the possible quantum jumps due to interaction with the environment, while the terms $\frac{1}{2} L_n^\dagger L_n \rho$ and $\frac{1}{2} L_n L_n^\dagger \rho$ are needed to normalize properly in case no jumps occur. Interaction of the qubit with the environment leads to two processes:

1. Relaxation: Decaying to the lower energy (ground) state $|0\rangle$ over time. In the block sphere picture, this means the tipping of the state vector toward the North Pole. The jump operator for relaxation is:

$$L_1 = \sqrt{\gamma_1} |0\rangle\langle 1| = \sqrt{\gamma_1} \begin{bmatrix} 0 & 1 \\ 0 & 0 \end{bmatrix} \quad (1.10)$$

Here, γ_1 is the relaxation rate. If initialized to $|\psi\rangle_i = |1\rangle$, the probability of finding the system in state $|1\rangle$ decays exponentially, with a time constant T_1 (inversely related to γ_1).

2. Dephasing: The loss of phase coherence of the qubit. This is most conveniently visualized in the Bloch sphere picture as an increasing uncertainty in the azimuthal angle ϕ of the Bloch vector. The jump operator for dephasing is:

$$L_2 = \sqrt{\gamma_2} \sigma_z = \sqrt{\gamma_2} \begin{bmatrix} 1 & 0 \\ 0 & -1 \end{bmatrix} \quad (1.11)$$

Here, γ_2 is the dephasing/decoherence rate. If initialized to $|\psi\rangle_i = \cos(\theta/2) |0\rangle + e^{i\phi} \sin(\theta/2) |1\rangle$ with well-defined phase ϕ , the uncertainty or fuzziness in the phase increases exponentially, with a time constant T_2 (inversely related to γ_2).

In practice, electron spin resonance (ESR) with pulsed AC magnetic fields can be used to execute single-qubit operations. Alternatively, electrically driven spin resonance

(EDSR), with pulsed AC electric fields in the presence of spin-orbit interaction or static magnetic field gradients, can be used. Non-entangling two-qubit unitary gate operations, i.e., ones that can be written as a direct product of single-qubit gates $U_{4 \times 4} = A_{2 \times 2} \otimes B_{2 \times 2}$ are just simultaneously driven single qubit operations (with different Larmor frequencies). The local static field or qubit g-factors are tuned such that the two qubits have different Larmor frequencies. Thus, driving one of the qubits at resonance has (almost) no effect on the other.

Entangling Gates

The exchange coupling between two spins in equation (1.1) can be tuned with gate voltages, allowing for the realization of entangling two-qubit gates. In the presence of a non-zero exchange interaction, a two-qubit CNOT operation can be executed using an AC pulse to selectively drive transitions of the target qubit only when the control qubit is in state $|1\rangle$ [fig 1.3]. Here, the system Hamiltonian in the $\{|00\rangle, |01\rangle, |10\rangle, |11\rangle\}$ basis is:

$$\hat{H}(J, B) = \frac{1}{2} \begin{bmatrix} -\Sigma g \mu_B B & 0 & 0 & 0 \\ 0 & -\Delta g \mu_B B - J & J & 0 \\ 0 & J & \Delta g \mu_B B - J & 0 \\ 0 & 0 & 0 & \Sigma g \mu_B B \end{bmatrix} \quad (1.12)$$

Here, $\Sigma g = g_1 + g_2$ is the sum of electron g-factors at the two sites, and $\Delta g = g_1 - g_2$ is the difference. J is the exchange interaction term. Again, the time evolution of the system driven at a particular frequency is obtained by solving the corresponding Lindblad master equation (1.9)¹.

Experimentally, the exchange interaction between spins confined in coupled quantum dots is controlled by varying the tunneling rate between the two quantum dots. In most cases, the oscillatory excitations are AC electric fields applied to the plunger or barrier gates of the corresponding quantum dot. Due to spin-orbit interaction, these AC electric fields are seen as oscillating magnetic fields by the electron spin. In the case of substrates without appreciable spin-orbit interaction, micromagnets are used

¹The jump operators in the two-qubit computational basis are constructed by taking the appropriate tensor product of single qubit collapse operators with identity and with one another (both qubits assumed to decohere at the same rate independently of one another).

to generate site-dependent magnetic field gradients, leading to a spin-orbit-like term in the Hamiltonian, allowing for full electric control of the spin qubit [20].

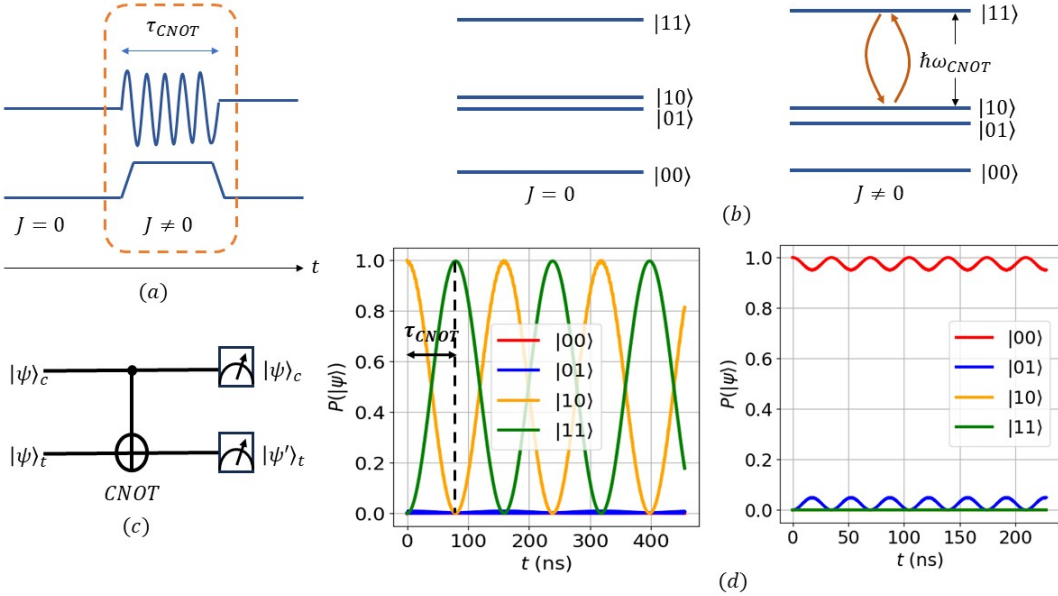


Figure 1.3: (a) Pulse sequence for executing a CNOT gate. The CNOT operation is executed by driving the qubit at ω_{CNOT} for a pulse duration of τ_{CNOT} . (b) Tuning of the two-qubit energy spectrum by controlling the exchange interaction J . (c) Circuit symbol: CNOT gate. (d) Occupation probability of the basis states vs duration of pulse: Qutip simulations for the time evolution of a two-qubit system (with exchange interaction) driven at $\hbar\omega_{CNOT}$. Here, a CNOT gate can be executed by choosing pulse duration τ_{CNOT} . Small amplitude off-resonance oscillations are seen even when the control qubit is in state $|0\rangle$, which can be eliminated by fine-tuning J and g -factors.

Simulation results in figure (1.3) and figure (1.2) are for a toy model of spins(s) in a DC field of 0.5T. An AC drive field at the appropriate frequency (depending on which two levels are driven) of amplitude 10mT is used to drive the two-level system. The decoherence rate γ_1 corresponding to $T_2^* \simeq 30\mu s$ used ($T_1 \sim 100T_2$). The g-factors are taken to be different ($g_1 = 1.95$ and $g_2 = 2.05$), assuming site-dependent modulation is possible and the effective mass to be $0.1m_e$, where m_e is the free electron mass. In figure (1.3), an exchange interaction J with strength equivalent to a Zeeman splitting at 0.02T is included in the Hamiltonian. Further interaction terms like spin-orbit terms, hyperfine, etc. can be simply added in the Hamiltonian [eq 1.12] to understand experimental results in specific cases.

Chapter 2

Device Structure

The fundamental design of gate-defined quantum dot devices in semiconductor heterostructures is derived from that of a MOSFET, with a key difference being the channel depth. Band bending at heterostructure interfaces of epitaxially grown GaAs|AlGaAs, Si|SiGe, and Ge|SiGe allow for the formation of a Quantum Well at a depth of $\sim 80\text{nm}$, $\sim 30\text{nm}$, and $\sim 30\text{nm}$ respectively, below the surface. Charge carriers in this buried Quantum Well have much better mobilities owing to significantly reduced scattering due to surface charges and a reduction in the overall electrical noise. In this work, we characterize quantum wells in both GaAs|AlGaAs and Si|SiGe heterostructures.

2.1 AlGaAs and SiGe

The conduction band offset at the heterostructure interface (fig 2.1 (b)) in the case of GaAs|AlGaAs leads to the formation of a 2D Electron Gas (2DEG), which is populated by electrons from the modulation-doped AlGaAs:Si layer. The extremely low lattice mismatch between GaAs and AlGaAs leads to high structural quality, thus allowing for electron mobilities $\sim 10^6 \text{ cm}^2/\text{Vs}$ at densities in the order of $\sim 10^{11} \text{ cm}^{-2}$. Confinement along the direction of growth (z-axis in fig 2.1) is a consequence of the band bending at the heterostructure interface, while the x-y confinement is modulated using surface gates by applying appropriate negative voltages to deplete the electron gas to form the quantum dot(s).

Band bending leads to the formation of a Quantum Well at the strained Silicon layer ($\sim 10\text{nm}$ thick) sandwiched between SiGe. Unlike AlGaAs, the heterostructure in this

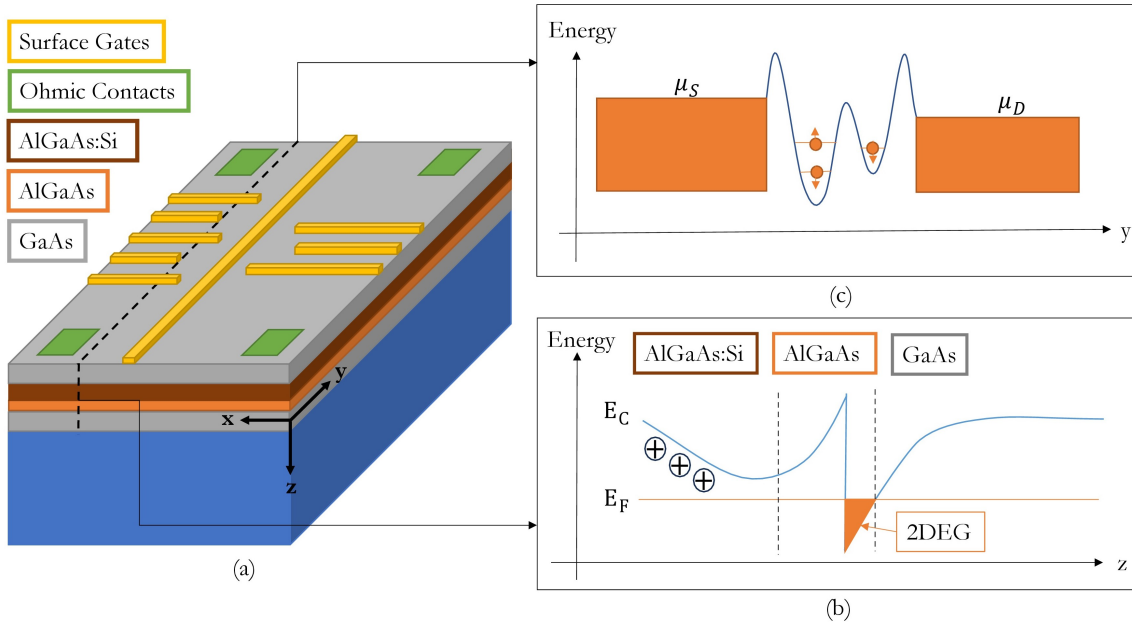


Figure 2.1: (a) A schematic of the structure for a GaAs|AlGaAs spin qubit device. (b) Band bending along the direction of growth. The quantum well formed at the AlGaAs|GaAs interface is populated by electrons from the Si-doped AlGaAs layer. (c) The potential landscape along the plane of the 2D electron gas is manipulated using surface gates.

case is undoped, and the well is not populated by default. Band bending due to an externally applied electric field (voltage on accumulation gates) leads to the formation of a 2DEG in the well. Due to the lattice mismatch between Si and Si_xGe_{1-x} with $x = 0.7$ the mobility of the 2DEG formed is lesser than in the case of AlGaAs, about $\sim 10^5 \text{ cm}^2/\text{Vs}$ at densities of the order of $\sim 10^{11} \text{ cm}^{-2}$.

The first spin qubits in semiconductor quantum dots were demonstrated in GaAs because of favorable band engineering and maturity of MBE growth. Another advantage is the appreciable spin-orbit interaction, which allows all-electric control of spin qubits. In terms of device fabrication, the realization of spin qubits in Si poses several challenges compared to GaAs. Firstly, due to the larger effective mass of electrons in the Si conduction band ($m_{||}^* = 0.19m_e$, $m_{\perp}^* = 0.98m_e$), for the same energy spacing, confinement in the plane of the 2DEG needs to be stronger than in the case of GaAs (with $m^* = 0.067m_e$), which translates to having smaller dot size in Si ($\sim 80\text{nm}$) compared to GaAs ($\sim 150\text{nm}$). From the fabrication point of view, the

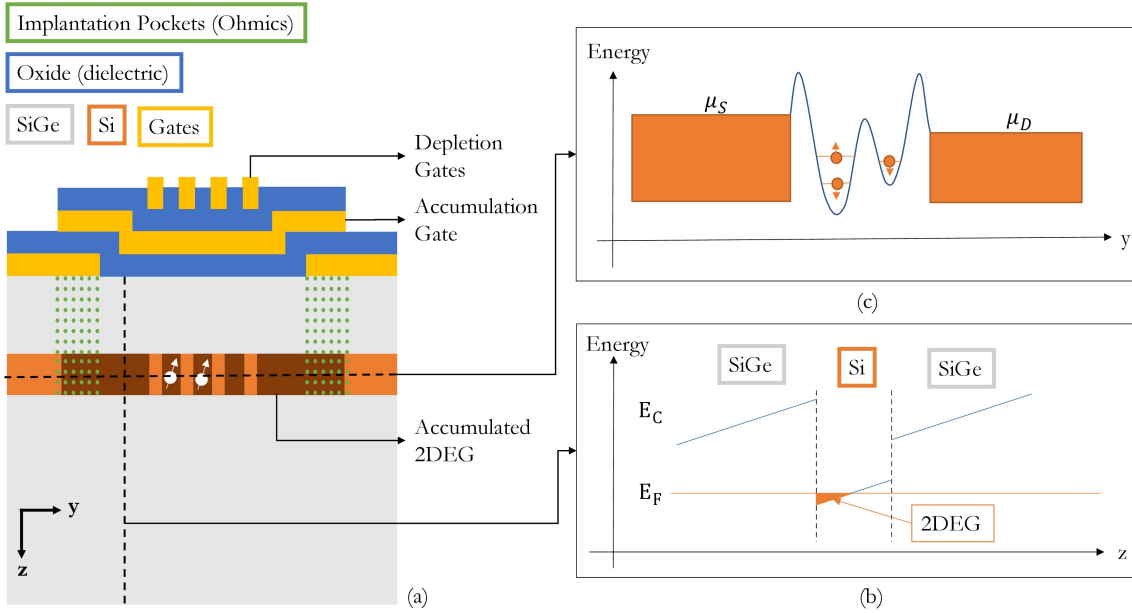


Figure 2.2: (a) A schematic of the cross-section of the structure for a Si|SiGe spin qubit device. (b) Band bending along the direction of growth. The quantum well is populated by electrons upon application of an external field. (c) The potential landscape along the plane of the 2D electron gas is manipulated using surface gates.

depletion gates used to confine electrons must be much narrower and more closely spaced in the case of Si. Furthermore, the oxide quality plays a detrimental role in the case of Si due to the requirement of multiple layers of gates for accumulation and depletion. Even with these bottlenecks, the field has moved to spin qubits in Silicon (and Germanium) due to CMOS compatibility and because of the higher relaxation and decoherence times of electron spins. This is a consequence of the absence of hyperfine interaction in isotopically purified ^{28}Si (zero nuclear spins), in contrast to III-V type heterostructures where hyperfine interaction leads to poorer T_1 and T_2 times.

2.2 Fabrication

Due to the single layer of gates, the steps involved in the fabrication process for the GaAs quantum dot device are a subset of that in SiGe. Processes for certain steps differ significantly due to the difference in material properties, Ohmic contacts being an example, in which case it is explicitly mentioned. Following is a summary of the key fabrication steps for the SiGe device [fig 2.3] without going into finer details:

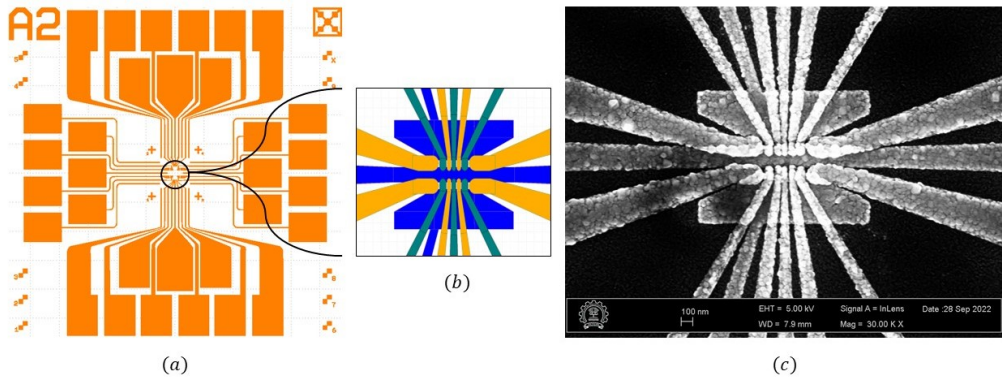


Figure 2.3: Si QD device: (a) Schematic layout of metallic gates. (b) Zoom in on the central region, showing the three layers of gates (confinement in blue, depletion in green, and accumulation in yellow). (C) SEM image of the Silicon Quantum dot device. Courtesy of Mr Siddarth Rastogi, QSi Lab, IIT Bombay. The device structure is adopted by the design by Xi Mi et al. [13]

1. Sample cutting and cleaning using RCA: a standard procedure for removal of organic residue from Si wafers.
2. Resist spinning followed by photo-lithography: the marker design pattern is written onto the wafer.
3. Metallization: Ti-Pd deposition on marker regions (using electron beam evaporation).
4. Liftoff: NMP removal at 70°C.
5. Resist spinning followed by photo-lithography: for ion implantation.
6. Phosphorous Ion implantation.
7. Resist removal using Plasma etching.
8. Annealing: Annealing to complete ion implantation (700°C for 15s with forming gas) by activation of Phosphorous donors to form ohmics.
9. Atomic layer deposition (ALD): 20 nm Al₂O₃ deposition.
10. Resist spinning followed by Photo-Lithography: ion implantation pockets left uncoated.
11. HF dip to remove oxide deposited on implantation pockets.

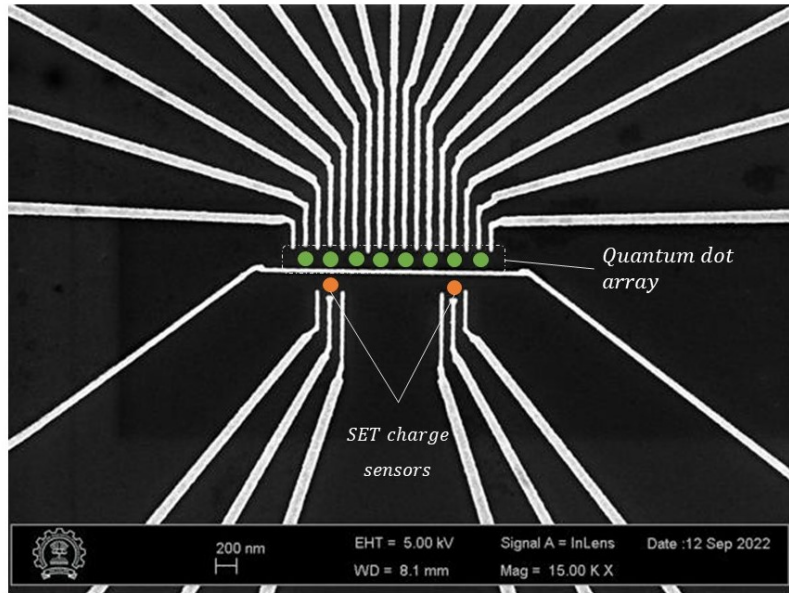


Figure 2.4: GaAs QD device: SEM image of fine gates written using electron beam lithography (EBL). Courtesy of Ms Varsha Jangir, QSi Lab, IIT Bombay. The device is an eight-dot array with two charge-sensing dots with the design adopted from the work by C. Volk et al. [19]

12. Metallization on implantation pockets.
13. Lift-off: NMP removal at 70°C.
14. Resist spinning followed by electron beam lithography (EBL) to write confinement gate pattern.
15. Metallization: Al deposition on gate pattern (using electron beam evaporation)
16. Lift-off: NMP removal at 70°C.
17. Thermal oxidation of $\sim 2\text{nm}$ Al_xO_y .
18. Steps 14 through 17 are repeated for accumulation and depletion gate layers.

In the case of GaAs, mesa etching is used to etch out regions besides the main device (fine gate and Ohmic area). Ohmic contacts are formed by metal diffusion (AuGe) till the depth of the quantum well, using annealing.

Chapter 3

Characterizing the Quantum Well

The parameters of this 2D electron gas (2DEG), like the carrier density (n), mobility (μ), and the contact resistance with the Ohmic pads (R_C) via implantation pockets, are crucial for transport measurements through quantum dots. The most ubiquitous technique to extract accurate values of these parameters is studying the transverse and longitudinal resistance of a Hall sample in the presence of magnetic fields. In this section, the focus is on experimental results and their analysis. A more rigorous discussion on the Quantum Hall effect can be found in the appendix A.

Lock-in Amplifiers (LIAs) are used for low noise measurements of transverse Hall voltage and longitudinal voltage showing Shubnikov-de Haas (SdH) oscillations. Frequencies (f) chosen for LI measurements are below 100Hz and are such that they are not integer multiples or factors of the 50Hz line frequency. The overall setup is similar to a standard 4-probe setup with the addition of pads to measure transverse voltage. Figure (3.1) is a schematic of the experimental setup. One LIA is used to supply source-drain current indirectly ($I_{SD} = \frac{V_{osc}}{2R_I}$) via a 1:1 isolation transformer and resistances R_I connected to the oscillator output (V_{osc}). $R_I = 10 M\Omega$ is chosen for our setup since it is much larger than the two-probe device resistance, making a near-ideal current source capable of sourcing up to 250 nA. The second LIA is “locked” to the reference signal of the source LIA. The two LIAs are used to record longitudinal ($V_{xx} = V_3 - V_1$) and transverse ($V_{xy} = V_5 - V_2$) voltages by measuring the voltage difference between two voltage pads in A-B mode. The time constant of the LIAs is set to be $\sim \frac{10}{f}$ s. The QDevil daughter board used for the above measurements has a low pass filter with $R_{filter} = 1.2 k\Omega$ and $C_{filter} = 1.0 nF$ on each DC line intended to

block RF noise.

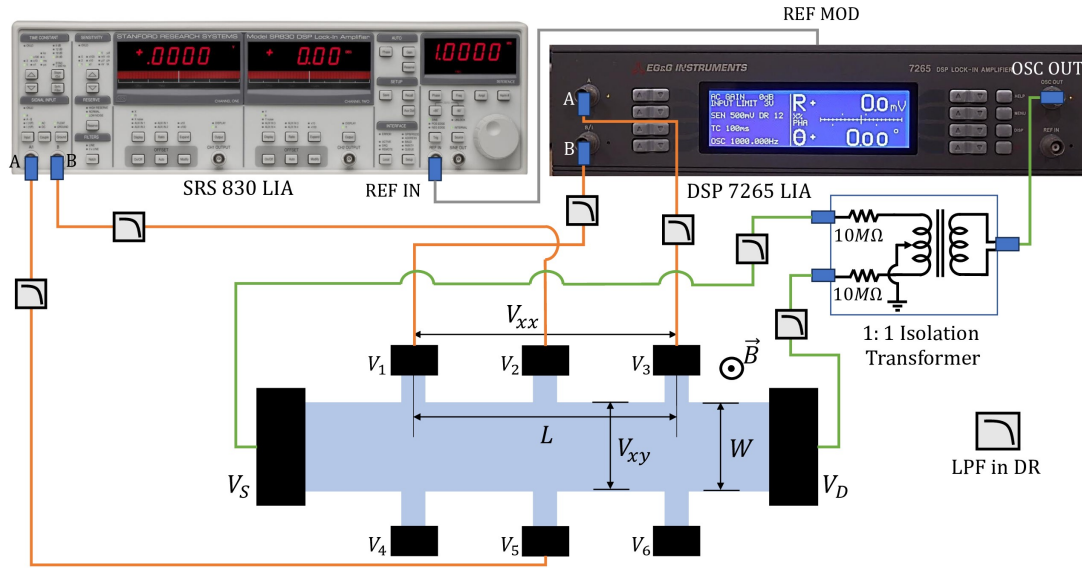


Figure 3.1: Experimental setup for Hall measurements using DSP 7265 and SR 830 LIAs. The Low Pass filter on the QDevil daughter board PCB has a $\frac{1}{R_{filter}C_{filter}} = 0.83 \text{ MHz}$, orders of magnitude higher than the LIA frequency.

3.1 GaAs|AlGaAs Hall Bar

Quantum Hall effect

Measurement setup for the Hall bar sample [fig (3.2)] is analogous to the one discussed above [fig (3.1)].¹ Two LIAs are used to measure transverse and longitudinal resistances. The source-drain current of amplitude 10 nA RMS, is set indirectly as in figure (3.2).

Quantum Hall and SdH measurement data from 0T up to 9T at different MXC temperatures was recorded. A clear temperature broadening of SdH peaks is seen as MXC temperature increases. Plateaus corresponding to integer filling factors $\nu = nh/eB$ [eq A.12] and some fractional filling factor values are observed. Peaks in R_{xx} coinciding with transitions between Hall plateaus are seen. The Klitzing constant

¹The measurements discussed in this section are done on a Hall bar sample provided by Professor Kanti May Dasgupta at IIT Bombay.

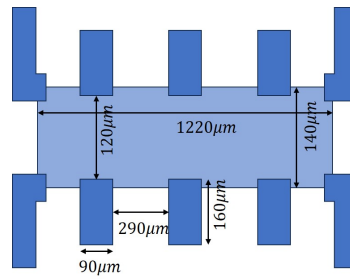


Figure 3.2: Hall sample geometry.

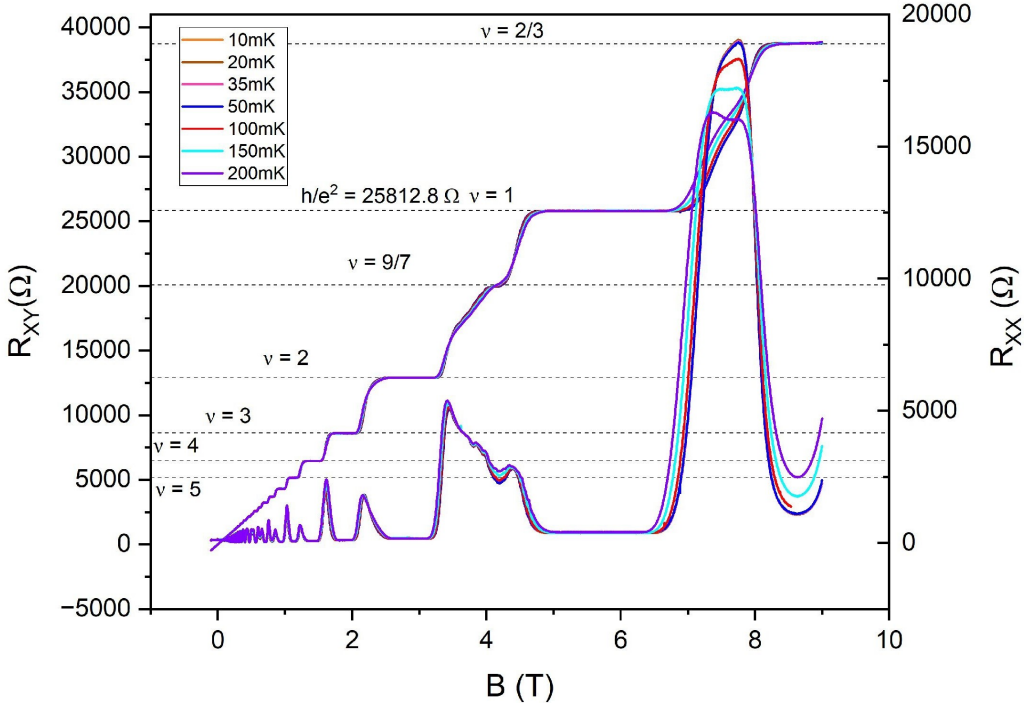


Figure 3.3: Hall and SdH data for a full 0-9T field sweep at different mixing chamber (MXC) temperatures.

[8] $R_K = 25.8128\text{k}\Omega$ (indicated on the plot) allows for the calculation of the actual sample current to be 9.471 nA.

Using the spin splitting of SdH oscillations, one can obtain the g-factor of the electrons in the 2DEG. At high fields, the Zeeman splitting becomes significant, and the spin degeneracy of Landau levels is broken. A Zeeman term needs to be added to the energy of Landau levels [eq A.14]:

$$E_q = \hbar\omega_c \left(q + \frac{1}{2} \right) \pm \frac{g\mu_B}{2} B \quad (3.1)$$

The R_{xx} jumps occur when a new Landau level starts filling, and the maxima is the

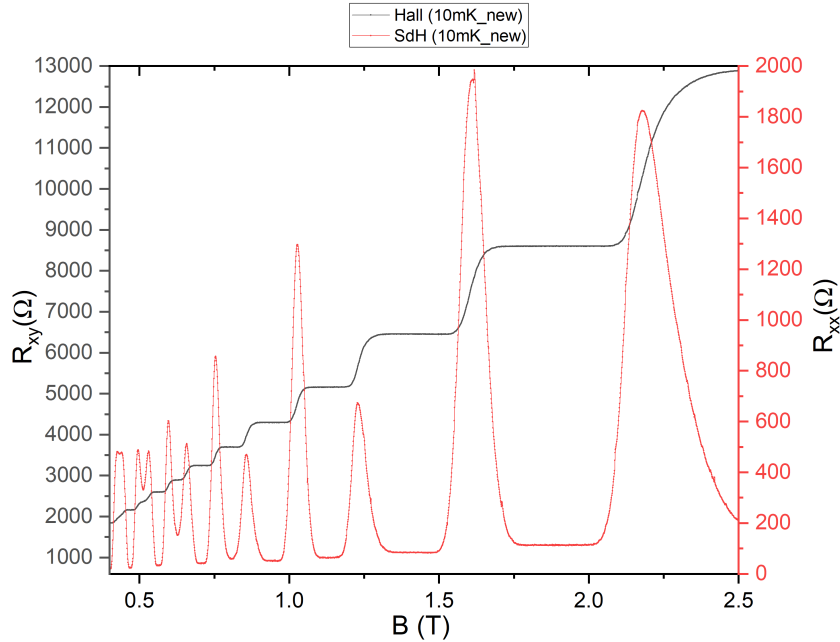


Figure 3.4: Zoomed in SdH and Hall data between 0.4T to 2.5T where spin splitting of Landau levels is apparent.

point when the Fermi energy E_F is equal to the Landau level energy E_q . Thus, the filling factor:

$$q = \alpha \frac{1}{B} - \frac{1}{2} \pm \Delta_s \quad (3.2)$$

Here, $\alpha = m^* E_F / e\hbar$ is a constant, and $\Delta_s = \frac{g m^*}{4m_e}$. Thus, plotting q (index of the Landau level being filled, i.e., filling factor ν) vs $1/B$ gives two straight lines with intercepts differing by $2\Delta_s$ [1]. For the data shown above, the g-factor was calculated to be 0.66 using $m^*/m_e = 0.067$. ¹

Electron Temperature

As the sample temperature reduces down to the mK regime, the electron-phonon coupling becomes weaker, and the effective electron temperature may differ from the actual lattice temperature, which is thermalized to the cold-finger. The SdH oscillations at intermediate magnetic fields can be used to extract the actual electron temperature using ‘‘Dingle fitting’’ as indicated in [6] and [7]. For intermediate fields,

¹This is roughly twice the expected value for GaAs, and thus, will be verified.

the amplitude of the SdH oscillations is obtained to be:

$$\Delta\rho_{xx} = 4\rho_0 \frac{\chi}{\sinh\chi} \exp\left[-\frac{\pi}{\omega_c\tau}\right] \quad (3.3)$$

$$\Rightarrow \ln(\Delta\rho_{xx}/4\rho_0) = \ln(\chi) - \ln(\sinh\chi) - \left[\frac{\pi}{\omega_c\tau}\right] \quad (3.4)$$

Here, $\rho_0 = m^*/ne^2\tau$ is the longitudinal resistance at zero field, and $\chi = 2\pi^2k_B T/\hbar\omega_c$ is a parameter that takes into account the effect of the electron temperature. Experimentally, we measure ρ_{xx} as a function of the magnetic field. From the Hall measurement, we can also extract the number density n . We then do a non-linear curve fit in accordance with equation (3.4) [fig 3.7] with two free parameters, namely τ the relaxation time and electron temperature T .

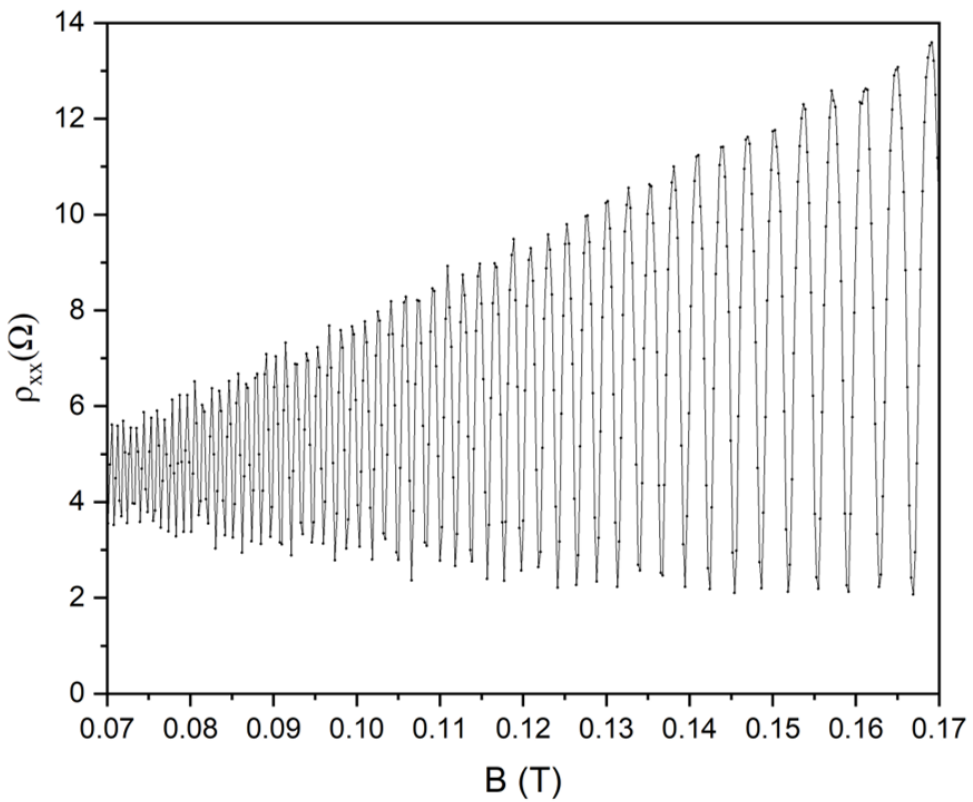


Figure 3.5: (a) Measured SdH oscillations. An envelope is fitted to this data using maxima and minima of the oscillations to obtain $\Delta\rho_{xx}$.

The thermalization of electrons with the lattice can be improved by increasing the number density of electrons in the 2DEG. In the case of GaAs—AlGaAs heterostructures, this can be done by exciting carriers trapped in the DX centers via infrared excitation. This is done using an infrared LED mounted on the coldfinger. A decrease

in $|T_{MXC} - T_{\text{electron}}|$ is observed post illumination.

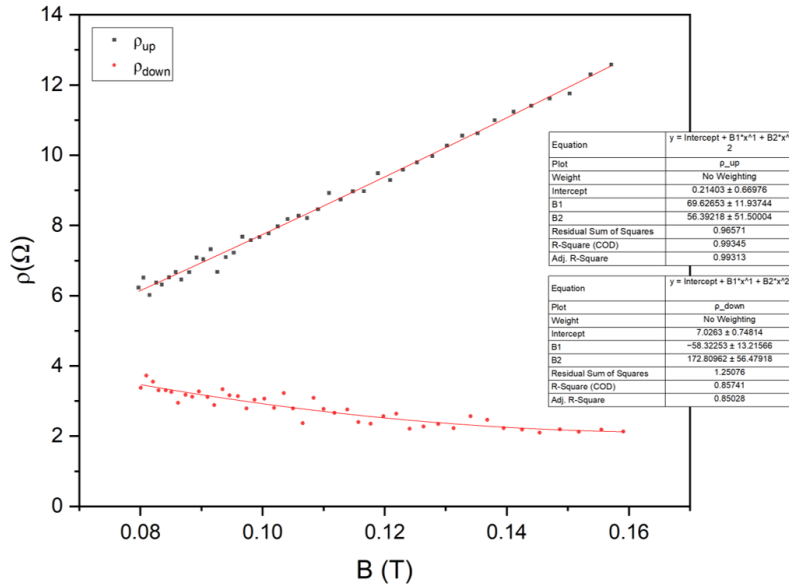


Figure 3.6: Envelope functions for the SdH oscillations (at 10mK) which are used to obtain ρ_{xx} .

Other sample parameters, namely the carrier density (n), and mobility (μ), are obtained from the low field Hall data. The slope of the Hall resistance R_{xy} vs field B gives the number density as $R_{xy} = B/ne$. The mobility $\mu = \frac{1}{\rho_0 ne}$ is then calculated using the zero field longitudinal resistivity $\rho_0 = R_{xx}(B = 0)W/L$. Here, $W = 140\mu m$ and $L = 670\mu m$. Measured values are (at 10mK MXC):

1. Prior to IR LED illumination: $n = 1.36 \cdot 10^{11} \text{ cm}^{-2}$ and $\mu = 1.78 \cdot 10^6 \text{ cm}^2/\text{Vs}$.
2. Post IR LED illumination: $n = 3.31 \cdot 10^{11} \text{ cm}^{-2}$ and $\mu = 4.67 \cdot 10^6 \text{ cm}^2/\text{Vs}$.

	Before Illumination				After Illumination		
	T_{MXC} (mK)	T_e (mK)	$T_e - T_{MXC}$ (mK)	τ (ps)	T_e (mK)	$T_e - T_{MXC}$ (mK)	τ (ps)
10	152.3	142.3	4.44	4.44	146.0	136.0	7.73
50	163.8	113.8	4.50	4.50	133.7	83.7	7.80
100	177.6	77.6	4.50	4.50	120.9	20.9	6.90
150	204.3	54.3	4.54	4.54	160.7	10.7	7.64
200	226.0	26.0	4.77	4.77			

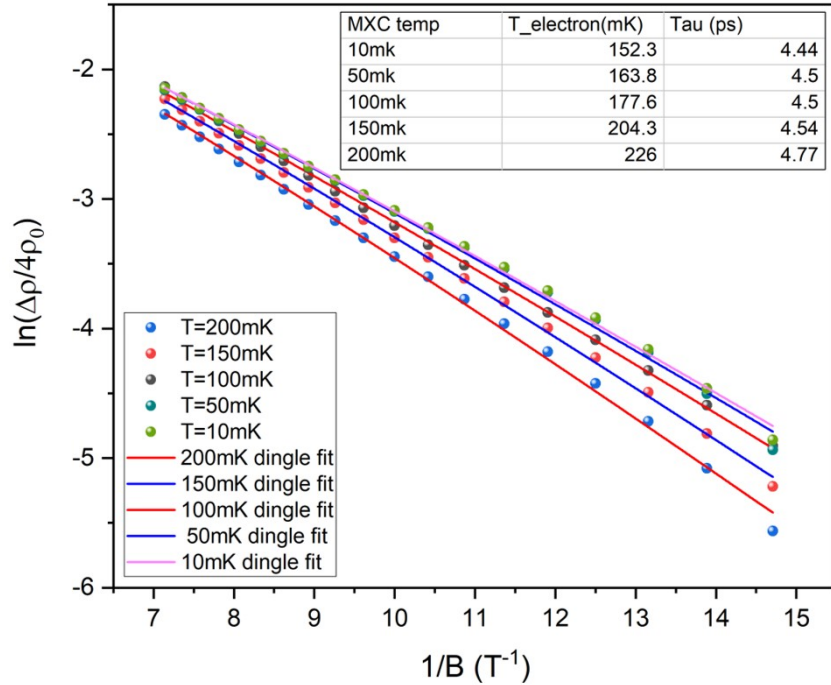


Figure 3.7: Electron temperature and relaxation time τ prior to illumination using Dingle fit.

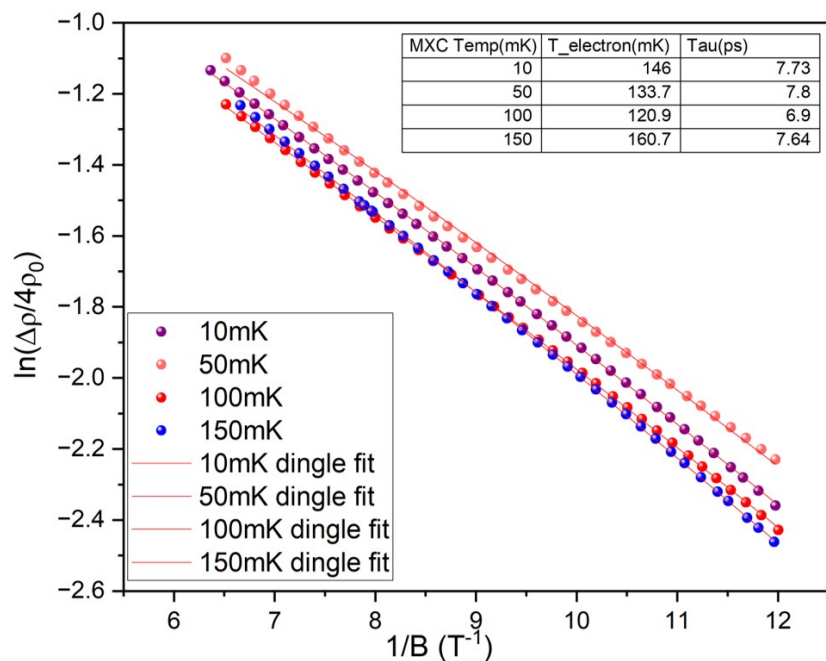


Figure 3.8: Electron temperature and relaxation time τ post illumination using Dingle fit.

3.2 Si|SiGe Hall Bar

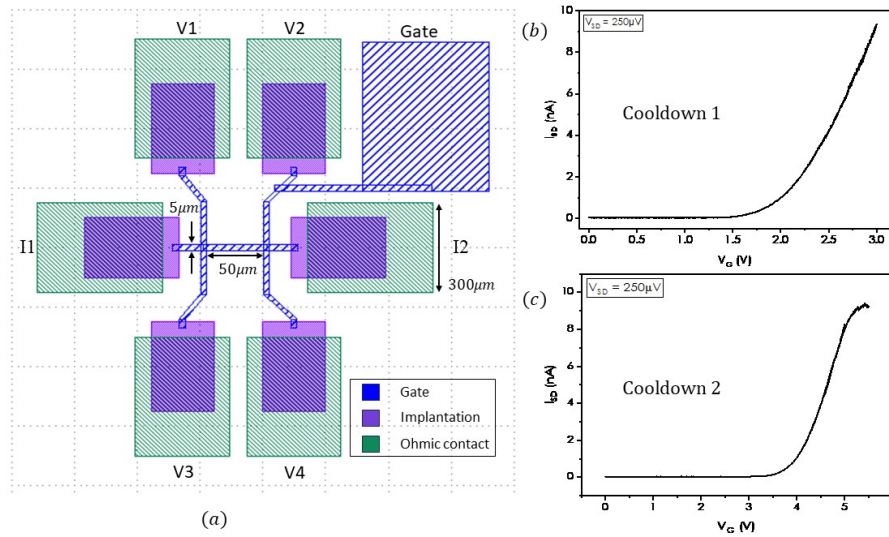


Figure 3.9: (a) SiGe Hall sample schematic. (b) and (c) Gate sweeps to determine turn-on voltage.

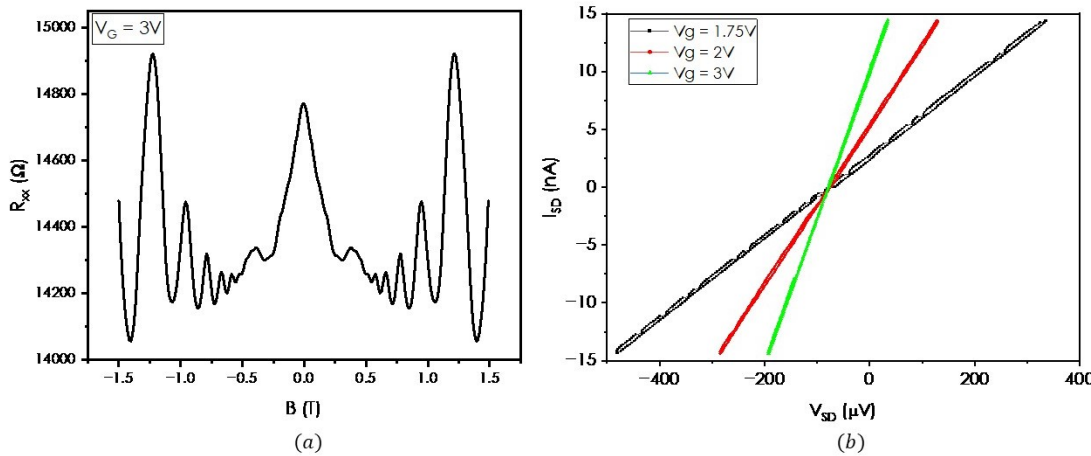
The sample was fabricated by Mr. Siddarth Rastogi at IIT Bombay. The fabrication steps are identical to those for the quantum dot device (2.2) up to the first layer (accumulation) of gates, with the main difference being the 80 nm SiO_2 deposited as the insulation in place of Al_2O_3 . Applying a positive voltage to the gate (V_g) leads to the accumulation of electrons in the buried quantum well.

First, a gate leak and short check are done before trying to accumulate the 2DEG by applying positive gate voltages. At $V_g = 0$, the contacts show an open circuit as expected, and at voltages higher than the turn-on threshold, the channel resistance drops with increasing gate voltage. The threshold voltage is obtained by measuring I_{sd} vs V_g with a constant V_{sd} . A few volts above the threshold, the channel current saturates w.r.t. gate voltage. Beyond this, increasing gate voltage does not induce more carriers in the well.¹

¹The sample had to be cooled down twice due to technical issues. The threshold voltage for channel formation is observed to shift from 1.5V for CD1 to 3.5V for CD2. Although not fully understood, this might be attributed to the rearrangement of trapped charges in the dielectric (oxide). In each cooldown (CD), the gate is “trained” by performing multiple V_g sweeps until the I_{sd} vs V_g curve is retraced every time.

V_g (V)	R_{2p} ($k\Omega$)	R_{4p} ($k\Omega$)	R_c ($k\Omega$)
1.75	109.13	28.51	37.41
2.00	48.19	14.52	13.94
3.00	29.07	7.93	7.67

Table 3.1: Two probe, four probe, and contact resistance for different gate voltages.

Figure 3.10: CD 1: (a) SdH oscillations at low magnetic field. (b) I_{sd} vs V_{sd} at various voltages higher than the threshold. The channel resistance progressively decreases with increasing gate voltage. Here, $R_{2p} = R_{4p} + 2R_c + R_{filter}$. $R_{filter} = 5.8 k\Omega$ is the resistance of the RF filter in the fridge.

The number density n and mobility μ are obtained from lock-in measurements of SdH oscillations in longitudinal resistance. The slope of low field Hall resistance could not be used for calculating n due to an intermixing of SdH in Hall owing to the smaller $W/L = 0.1$ than desirable. This design issue is fixed in future iterations of similar samples. The number density can be found from the periodicity in $1/B$ of the SdH oscillations [equation (A.21)], and this, combined with the zero-field longitudinal resistivity ρ_{xx} value, gives electron mobility μ .

For CD 1, at 3V gate voltage, $n = 2.1 \cdot 10^{11} \text{ cm}^{-2}$ and $\mu = 2.02 \cdot 10^4 \text{ cm}^2/\text{Vs}$. For CD 2, a more detailed study of n and μ as a function of gate voltages was done. The measurements reveal that the charge accumulation in the quantum well is successful, and the number density can be varied in a small range before saturation by varying

the gate voltage.

V_g (V)	R_{2p} ($k\Omega$)	R_{4p} ($k\Omega$)	R_c ($k\Omega$)	n (10^{11}cm^{-2})	μ ($10^4\text{cm}^2/\text{Vs}$)
5.2	148.41	31.40	31.40	1.64	55.61
5.4	82.47	22.59	27.04	1.72	1.60
5.6	50.67	15.63	14.62	1.88	2.13
5.8	34.63	10.49	9.17	2.15	2.78
6.0	25.71	7.02	6.45	2.41	3.69

Table 3.2: Two probe resistance, four probe resistance, contact resistance, number density, and mobility for different gate voltages.

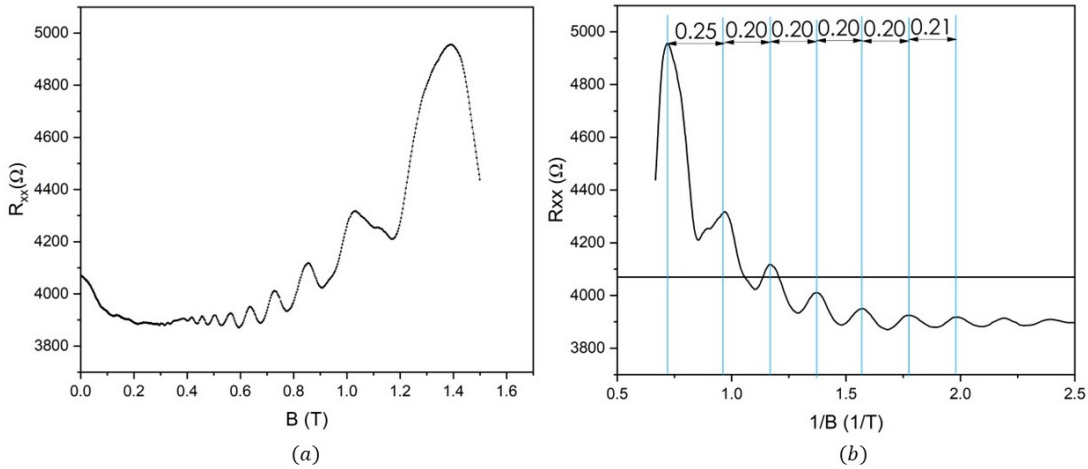


Figure 3.11: Cool down 2: (a) SdH oscillations at $V_g = 6\text{V}$. (b) Finding periodicity of R_{xx} in $1/B$ to get n .

The measurements discussed above demonstrate that the Phosphorous implantation for establishing Ohmic contacts works as intended. The channel resistance and carrier density are in the expected range, but the mobility value is smaller than expected. Although not detrimental to transport measurements through quantum dots, optimization of this might be possible by depositing higher quality oxide of lesser thickness.

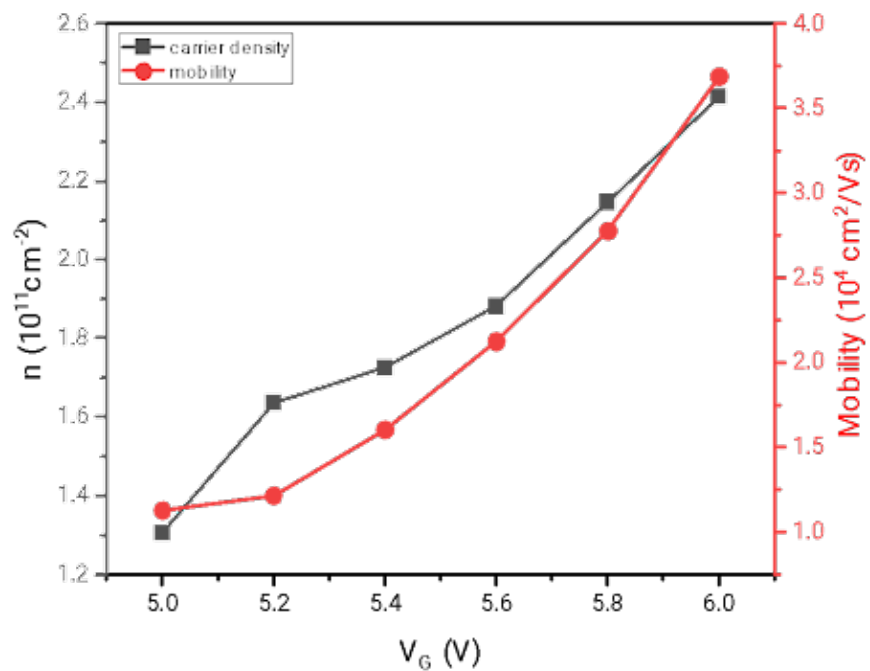


Figure 3.12: CD 2: Variation of n and μ with gate voltage.

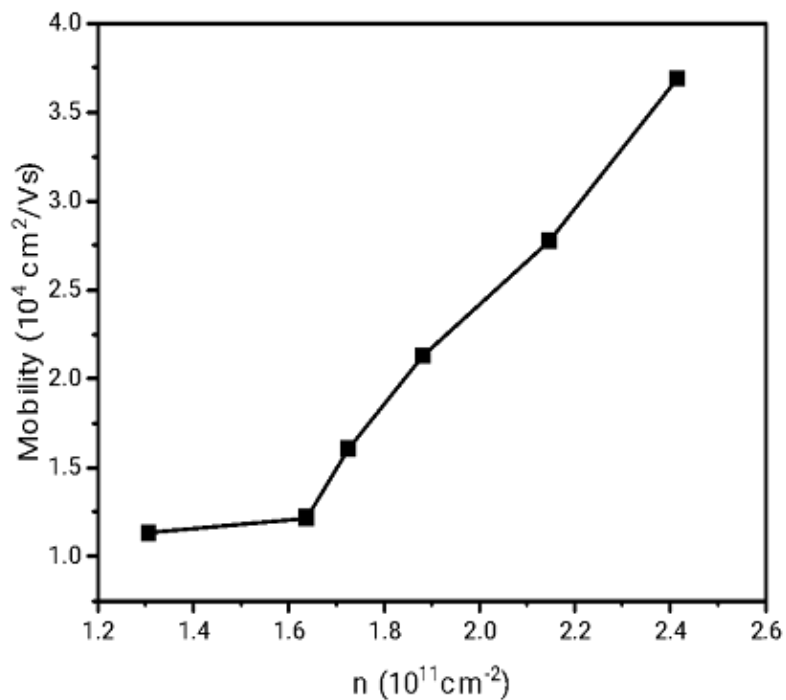


Figure 3.13: CD 2: μ vs n .

Chapter 4

Transport Through Quantum Dots

4.1 The Constant Interaction Model

A quantum dot is an artificial 3D confinement of electrons in a region of size $\sim 100\text{nm}$ (for semiconductor quantum dots). The de Broglie wavelength of these electrons is comparable to the size of the dot, and the electrons occupy discrete quantum levels similar to orbitals in atoms that have a discrete excitation spectrum. Such a quantum dot can be modeled as an island of a finite number of electrons coupled to two reservoirs and a gate, which is used to manipulate the charge state of the quantum dot.

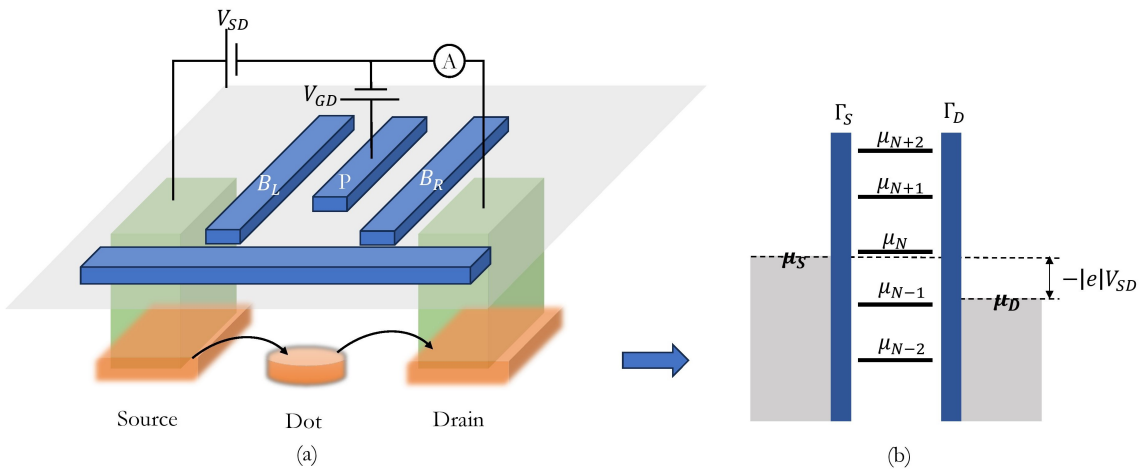


Figure 4.1: (a) Schematic showing the setup for transport measurements across a lateral gate-defined quantum dot. (b) The Plunger gate (P) voltage V_g lowers or raises the electrochemical potential ladder of the dot. The tunnel couplings to the reservoirs Γ_s and Γ_d are controlled by the Barrier (B_L and B_R) gate voltages.

The transport through a quantum dot can be understood using the Constant Interaction model [9]. The model is based on two assumptions. First, the interactions of electrons in the quantum dot with the environment are captured by a single effective capacitance $C_{\Sigma} = C_g + C_s + C_d$, where C_g is the capacitive coupling with the gate, C_s to the source, and C_d to the drain. Second, the single-particle energy spectrum of the dot is independent of the number of electrons. In that case, the energy of the dot filled with N electrons is given by:

$$U(N) = \frac{[-|e|(N - N_0) + C_s V_s + C_d V_d + C_g V_g]^2}{2C_{\Sigma}} + \sum_{n=1}^N E_n(B) \quad (4.1)$$

Here, $-|e|$ is the electronic charge, and N_0 is the number of electrons at zero gate voltage. $E_n(B)$ is the n^{th} single particle energy state in the presence of an external magnetic field B . The terms $C_i V_i$ ($i = g, s, d$) are effective induced charges due to a change in the electrostatic potential of the dot. The above expression can be modified to include couplings with other gates and the 2DEG.

The electrochemical potential of the dot is defined as:

$$\mu_{N-1 \leftrightarrow N} = U(N) - U(N-1) = E_N(B) + \frac{e^2}{C_{\Sigma}} \left(N - N_0 - \frac{1}{2} \right) - \frac{e}{C_{\Sigma}} (C_g V_g + C_s V_s + C_d V_d) \quad (4.2)$$

$$\begin{aligned} \mu_{N-1 \leftrightarrow N} &= E_N + E_C \left(N - N_0 - \frac{1}{2} \right) - \frac{E_C}{e} (C_g V_g + C_s V_s + C_d V_d) \\ &= E_N + E_C \left(N - N_0 - \frac{1}{2} \right) - e \sum_i \alpha_i V_i \end{aligned} \quad (4.3)$$

Here, E_C is the charging energy of the dot and $\alpha_i = \frac{C_i}{C}$ is the “lever arm” of the i^{th} gate electrode. The energy required to add the N^{th} electron, termed as the addition energy, is given as:

$$E_{add}(N) = \mu_{N \leftrightarrow N+1} - \mu_{N-1 \leftrightarrow N} = E_C + \Delta E \quad (4.4)$$

This is the energy difference between ground-state electrochemical potentials. Here, $\Delta E = E_{N+1} - E_N$ is the energy difference between the consecutive electron states, which can be zero in case electrons are added to the same spin-degenerate level. Excited states can also contribute to transport through the dot with associated electrochemical potentials:

$$\mu_{i \leftrightarrow j} = U_i(N) - U_j(N-1) \quad (4.5)$$

Here, i and j are used to index the states, with primes denoting excited states; for example, the electrochemical potential corresponding to the transition between the N electron ground state and the $N + 1$ electron excited state is $\mu_{N \leftrightarrow (N+1)'}^+$.

4.2 Coulomb Spectroscopy

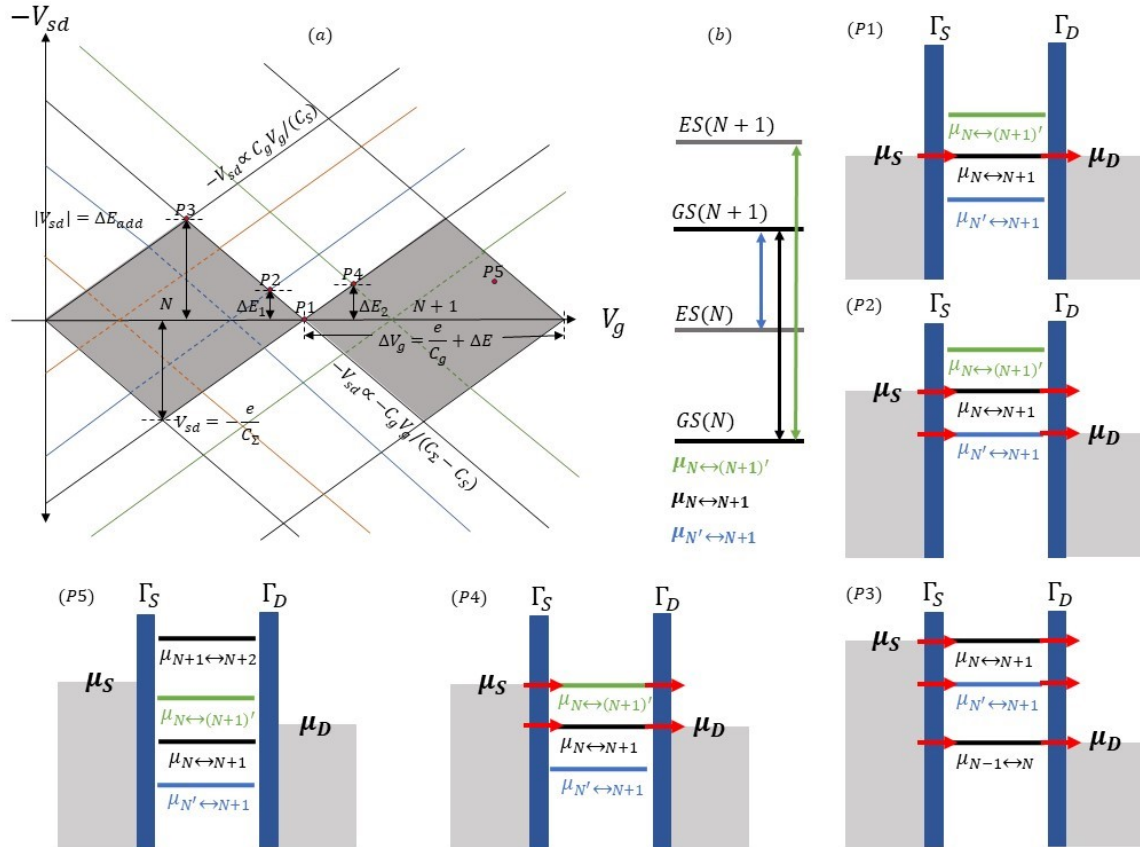


Figure 4.2: (a) A schematic of the quantum dot conductance as a function of the source-drain bias (V_{sd}) and plunger voltage (V_g). (P1) Low bias regime: transport through the dot occurs only when $\mu_{N \leftrightarrow N+1}^+$ aligns with μ_s and μ_d [5]. (P2), (P3), (P4), (P5) High bias regime: excited states may participate in transport, leading to higher current through the dot. The transitions involving excited states are allowed only when the respective electrochemical potential corresponding to the ground-to-ground state transition lies in the bias window. The dot is in “Coulomb blockade” (grey area) when none of the electrochemical potentials corresponding to ground state transitions between two dot occupancies lies in the bias window.

Transport through the quantum dot is possible if at least one chemical potential

corresponding to a ground state N to ground state $N + 1$ transition lies within the bias window, i.e., $\exists N$, such that $\mu_s \geq \mu_{N \leftrightarrow N+1} \geq \mu_d$, with the magnitude of current determined by the tunneling rates Γ_s and Γ_d . At the “Coulomb peaks”, the dot occupancy fluctuates between two or more charge occupancies, thus leading to the current. Otherwise, the dot is said to be Coulomb blockade, and the occupancy of the dot remains unchanged. For a fixed low source-drain bias ($eV_{sd}, k_B T \ll E_C$), this manifests as peaks in dot current at specific gate voltages. In the case of high source-drain bias, multiple electrochemical potential levels can participate in transport, allowing for transport via multiple parallel channels.

A 2D plot of dot current (or conductance) as a function of bias and gate voltages allows one to extract several parameters characterizing the quantum dot [fig 4.2]. The regions where the dot is in Coulomb blockade form the so-called Coulomb diamonds in the V_g - V_{sd} space. In the following discussion, the drain is assumed to be held at a constant zero potential ($V_d = 0 \Rightarrow \mu_s = -eV_{sd}$), which is the reference with respect to which all other voltages are applied. For low bias, i.e., $V_{sd} = 0$, current across the dot is non-zero when:

$$\mu_{N \leftrightarrow N+1} = E_{N+1} + E_C \left(N - N_0 + \frac{1}{2} \right) - \frac{E_C}{e} (C_g V_g + C_s V_s + C_d V_d) = \mu_s \quad (4.6)$$

This means that, as the gate voltage V_g is swept (keeping $V_{sd} = 0$), the current through the dot shows peaks separated by $\Delta V_g = e/C_g + \Delta E$, where $\Delta E = E_{N+1} - E_N$ if the peaks correspond to $\mu_{N \leftrightarrow N+1}$ and $\mu_{N-1 \leftrightarrow N}$.

When the source chemical potential $\mu_s > \mu_d$ aligns with a level corresponding to a dot transition, say $\mu_{N \leftrightarrow N+1}$ then:

$$\mu_s = -eV_{sd} = E_{N+1} + E_C \left(N - N_0 + \frac{1}{2} \right) - \frac{E_C}{e} (C_g V_g + C_s V_{sd}) \quad (4.7)$$

$$\Rightarrow -V_{sd} = -\frac{C_g}{C_\Sigma - C_s} V_g + \lambda \quad (4.8)$$

Thus, in the $-V_{sd}$ vs V_g space, this is a straight line with slope $-C_g/(C_\Sigma - C_s)$. Similarly, the slope of the line corresponding to $\mu_d = 0 = \mu_{N-1 \leftrightarrow N}$ is C_g/C_s . Clearly, lines corresponding to a new dot potential level aligning with one of the reservoirs will have the same slope as one of the two lines above, just different intercepts.

Point P3 in figure (4.2) corresponds to the $\mu_{N \leftrightarrow N+1}$ aligning with μ_s , and $\mu_{N-1 \leftrightarrow N}$ with μ_d . The source drain bias times the electronic charge ($|eV_{sd}|$) at P3 gives the addition energy $E_{add}(N) = \mu_{N \leftrightarrow N+1} - \mu_{N-1 \leftrightarrow N}$. Similarly, excitation energy can be calculated based on the bias voltage at certain intersections in the charge stability diagram. For instance, for the point P2 in figure (4.2) $\mu_{N \leftrightarrow N+1}$ is aligned with μ_s , and $\mu_{N' \leftrightarrow N+1}$ with μ_d , thus, $|eV_{sd}| = E_{N'} - E_N$.

In the absence of a magnetic field, any orbital state of the dot is two-fold spin degenerate, i.e., the state is equally likely to be filled with a spin-up \uparrow or a spin-down \downarrow electron. Contrary to this, if the magnetic field is switched on, this degeneracy is broken, and the charge transition lines in the charge stability diagram split into two. For example, the transition line joining P1, P2, and P3 in figure (4.2) would split in two. What was earlier $\mu_{N \leftrightarrow (N+1)}$ now splits to $\mu_{N \leftrightarrow (N+1)\downarrow}$ and $\mu_{N \leftrightarrow (N+1)\uparrow}$ differing in energy by $g\mu_B B$. In this case, the excitation energy ($\mu_{N \leftrightarrow (N+1)\uparrow} - \mu_{N \leftrightarrow (N+1)\downarrow} = \Delta E_z = g\mu_B B$) obtained from the Coulomb spectroscopy is field dependent. Most importantly, a measurement of ΔE_z vs magnetic field gives a straight line with slope $g\mu_B$, thus giving the material g -factor. In an exactly analogous manner, one can extract the field-dependent spin splitting, say, for example, in the singlet-triplet states for a dot occupancy of $N = 2$.

4.3 Tunnel Barriers and Electron Temperature

We consider a simplistic model [2] describing the transport through a really small channel (our quantum dot) coupled to two electron reservoirs with a small bias voltage applied: small enough that only a single electrochemical potential lies within the bias window. A constant difference in the source-drain electrochemical potentials is maintained by an external voltage source: $\mu_s - \mu_d = -eV_{sd}$. If N electrons in steady state (net zero current flux $I_s = -I_d$) occupy the dot, and $f_s(\mu) = f_{FD}(\mu - \mu_s)$ and $f_d(\mu) = f_{FD}(\mu - \mu_d)$ are the reservoir Fermi functions, then the current fluxes through each contact are¹:

$$I_s = e\Gamma_s(f_s - N), \quad I_d = e\Gamma_d(f_d - N) \quad (4.9)$$

$$N = \frac{\Gamma_s f_s + \Gamma_d f_d}{\Gamma_s + \Gamma_d} \quad (4.10)$$

¹ignoring broadening of dot level around μ due to finite lifetime τ

$$I = I_s = -I_d = e \frac{\Gamma_s \Gamma_d}{\Gamma_s + \Gamma_d} (f_s - f_d) \quad (4.11)$$

The tunneling rates Γ_s and Γ_d give the rate at which an electron tunnels into the dot from the source or out to the drain from the dot, respectively. No current flows when a level μ is much above (below) both μ_s and μ_d since $f_s(\mu) = f_d(\mu) = 0$ ($f_s(\mu) = f_d(\mu) = 1$). Transport through the dot is only possible if μ lies within a few $k_B T$ of μ_s and μ_d , i.e., when $\mu_s > \mu > \mu_d$. For symmetric tunneling rates $\Gamma = 2\Gamma_s = 2\Gamma_d$, the current value at the Coulomb peak ($\mu_s > \mu > \mu_d$, thus $f_s \simeq 1$ and $f_d \simeq 0$) allows one to experimentally extract Γ . For gate-defined quantum dots, Γ is highly tunable using barrier gate voltages. Coupling of the dot with the reservoirs leads to a finite lifetime of the electron in the dot ($\tau \sim \Gamma^{-1}$). This can be seen as a broadening of the Coulomb peak due to the DOS in the dot spreading out around μ . In the simplest case, this is a Lorentzian about $E = \mu$:

$$D_\mu(E) = \frac{1}{\pi} \frac{\Gamma \hbar / 2}{(E - \mu)^2 + (\Gamma \hbar / 2)^2} \quad (4.12)$$

Here, $\Gamma = \Gamma_s + \Gamma_d$. The corresponding current and dot occupation are:

$$I = e \int_{\mu_d}^{\mu_s} dE D_\mu(E) \frac{\Gamma_s \Gamma_d}{\Gamma_s + \Gamma_d} (f_s - f_d) \quad (4.13)$$

$$N = \int_{-\infty}^{+\infty} dE D_\mu(E) \frac{\Gamma_s f_s + \Gamma_d f_d}{\Gamma_s + \Gamma_d} \quad (4.14)$$

For small bias and low temperatures $f_s(E) - f_d(E) \simeq 1$ iff $\mu_s > E > \mu_d$, else 0. So, the current profile of the Coulomb peak is a Lorentzian with FWHM = $(\Gamma_s + \Gamma_d)\hbar$ instead of a sharply peaked delta function along $e\alpha_P V_P$ axis.

Broadening of Coulomb peaks is caused due to two effects: broadening of the dot level associated with the finite lifetime of the electron in the dot and the Fermi distribution of the reservoirs at finite temperature ($f_{FD}(E - \mu_{res}, T_{res})$). Now, consider a case when $\hbar\Gamma \ll k_B T \ll |eV_{sd}| < E_{add}$. This is when the bias window is larger than a few $k_B T$, which is, in turn, larger than the energy broadening $\hbar\Gamma$ of the dot state (Lorentzian broadening can be ignored). Now in equation (4.11), when the dot potential μ is nearly aligned to the source (drain) potential μ_s we have $\mu \gg k_B T + \mu_d \Rightarrow f_d(\mu) = 0$ (μ_d and $\mu + k_B T \ll \mu_s \Rightarrow f_s(\mu) = 1$). The current profile then traces the Fermi-Dirac distribution of the corresponding reservoir (at temperature T_{res}) when the dot potential is near the Coulomb peak flanks [12]:

$$I = e\Gamma \left[\exp \left(\frac{e\alpha_P(V_P - V_{P0})}{k_B T_{res}} \right) \right]^{-1} + I_0 \quad (4.15)$$

α_P is the plunger gate (of QD) lever arm, V_{P0} the plunger offset voltage, and I_0 the current offset.

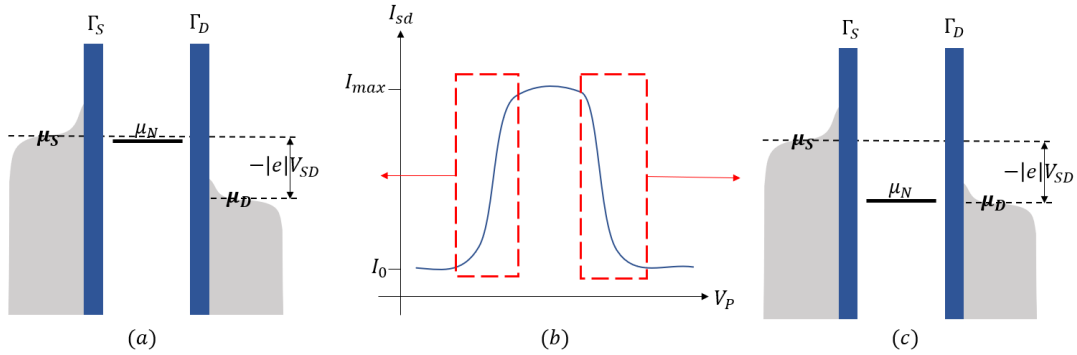


Figure 4.3: Schematic showing the electrochemical potential alignment near the two flanks of the Coulomb peaks. The profile of the dot current traces the Fermi function. The barriers, plunger gate, and the source-drain bias are tuned to a regime where $\hbar\Gamma \ll k_B T \ll |eV_{sd}| < E_{add}$.

Chapter 5

T₁ and T₂ Measurement

Before moving to the experimental techniques used for determining T₁ (relaxation time) and T₂ (decoherence time), we must establish techniques to reliably read the charge and the spin state of the quantum dot.

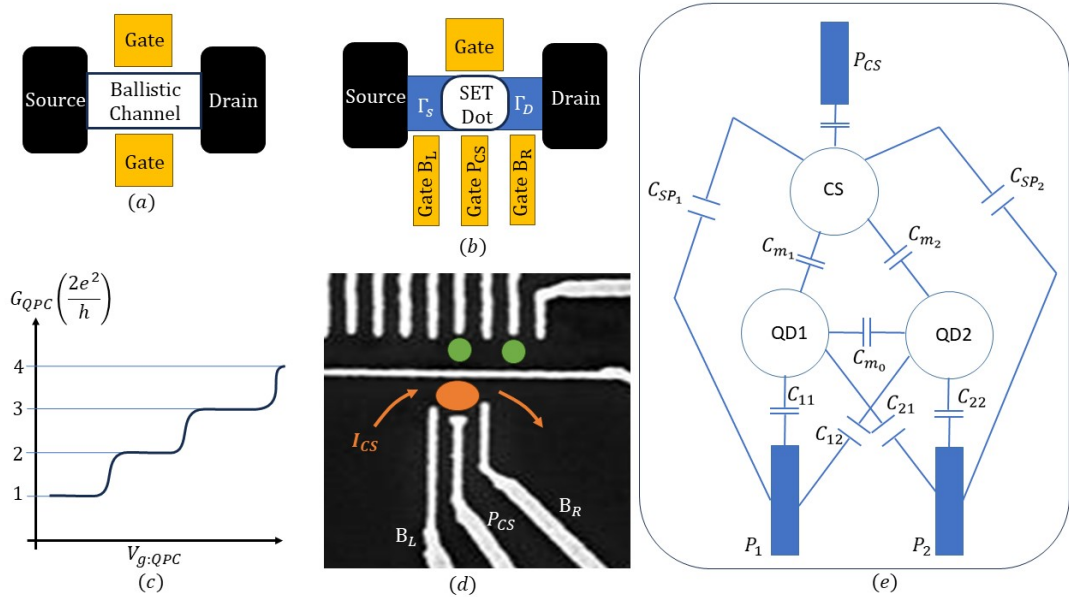


Figure 5.1: (a) and (b) Schematics of a QPC (modeled as a ballistic channel with gate tunable width) and SET quantum dot-based charge sensors. (c) Schematic of conductance quantization for a QPC. (d) SET charge sensor in GaAs|AlGaAs device. (e) Schematic showing various capacitive couplings in the system of a double quantum dot and a SET charge sensor. The barrier gate voltages are assumed to be at a constant voltage and thus not shown.

5.1 Charge Sensing

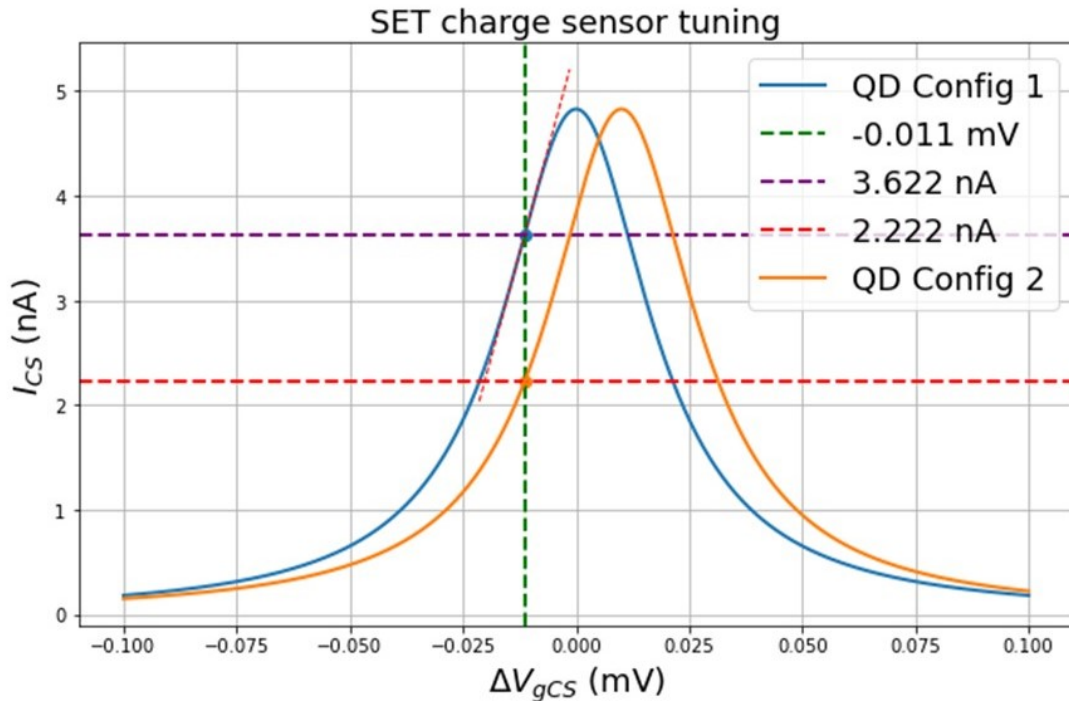


Figure 5.2: Tuning a SET charge sensor: SET gate voltage is chosen to be at the Coulomb peak flank. The sensitivity of the sensor is maximum on the flank where the slope of the current profile is maximum. Sudden charge jumps in coupled quantum dots can effectively be seen as a shift in the Coulomb peaks, leading to a different SET current.

A technique different from the transport measurements discussed above is needed in many cases. Direct transport measurement through quantum dots faces some fundamental problems. Firstly, it cannot be used to sense the charge state of dots coupled to a single reservoir. This means it cannot be employed for measurements on an array of more than two dots. Another problem is that detecting measurable current across a dot needs the tunnel barriers to be below a certain value (for appreciable tunneling rates Γ_s and Γ_d). Because of the capacitive effect of the plunger gate on tunnel barriers, detecting currents below a certain dot occupancy may become a non-trivial task of tuning gate voltages. This may be an issue when depleting down to the last electron.

Indirect charge sensing can be realized by using a quantum point contact (QPC) or a single electron transistor (SET) coupled to the quantum dot(s) whose charge state needs to be measured. The underlying principle is the effect of the capacitive coupling

between the charge sensor (QPC or SET) with the quantum dot. In the case of a SET, the SET dot's electrochemical potential ladder is extremely sensitive to changes in the electrostatic profile near the dot. Jumps in the charge of a coupled quantum dot cause an appreciable change in SET current when tuned to a flank of a Coulomb peak, which forms the signal indicating the charge state of the dot. Similarly, transitions between conductance plateaus of a QPC can be used as sensitive electrometers. For both GaAs and SiGe devices, we have SETs as charge sensors.

5.2 Elzerman Spin readout (ERO)

Spin-to-charge conversion is used to read out the spin of an electron in a quantum dot. Here, we focus on the ERO [4] and Pauli Spin Blockade (PSB) [10]. ERO uses a four-step pulse sequence to read out the spin state based on different electrical responses for the two spin states owing to selective tunneling possible for the \downarrow spin state in the read-out part of the sequence.

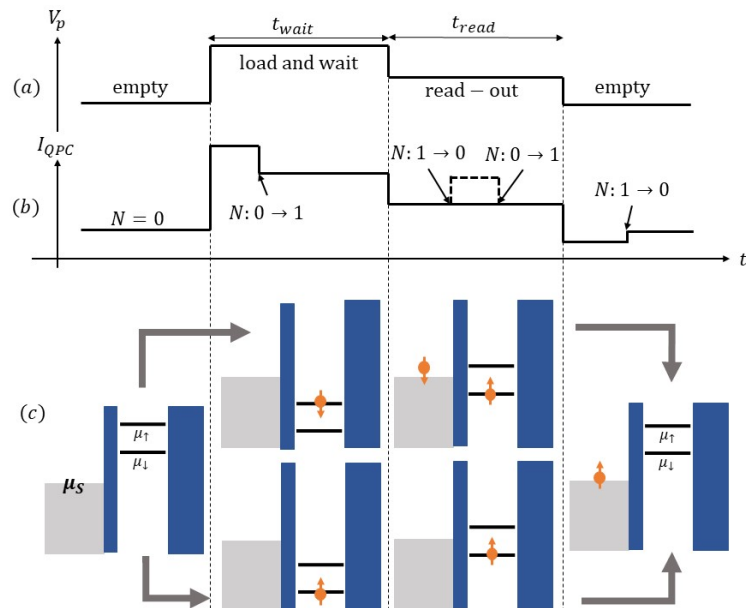


Figure 5.3: Schematic for ERO (a) Pulse sequence applied to the quantum dot plunger gate to raise/lower the electrochemical potential ladder. (b) Response of a QPC charge sensor: responds to charge jumps as well as plunger voltage changes. The signal obtained in case a spin-up electron (dotted) is loaded shows an added jump in the read-out step. This jump is seen when the spin-down electron tunnels out and a spin-up electron is filled. (c) Schematic of the dot configuration.

5.3 T₁ Measurement using ERO

A pulse scheme very similar to the one described in figure (5.3) can be used to measure T₁, the relaxation time constant for the higher energy spin-down ↓ state of the electron in a dot [17].

The first step loads an electron into the excited state with a certain probability p_0 , or into the ground state with probability $(1 - p_0)$ which can be determined. This is followed by waiting at the same voltage, during which if the electron is in the excited state and survives the wait-time without decaying to the ground state, a jump in signal is seen in the read-out pulse when ↓ tunnels out, and a ↑ is loaded. The third step unloads ↑ to empty the dot. Measurements of the signal over several such pulse sequences are averaged to get a signal. The average value of the jump in the read-out part is measured for different wait times. With increasing wait-time t_{wait} , the fraction of instances when a jump is seen during the read interval will decay exponentially as $p = p_0 e^{-t_{wait}/T_1}$ (assuming that the $T_1 \gg 1/\Gamma$, Γ being the tunneling rate to the lead). The jump signal average vs t_{wait} , shows an exponential decay with a time constant equal to the spin-lattice relaxation time T₁.

Chapter 6

Quantum Transport Measurement Setup

6.1 Dilution Refrigerator

Working Principle

Joule-Thomson cooling is a phenomenon where the temperature of a gas drops due to sudden expansion, often after being forced through a small constriction at high pressures. This, combined with evaporative cooling, are commonly used techniques in refrigeration and cooling. Pumping on a liquid coolant can be used to achieve temperatures lower than its boiling point using evaporative cooling; for instance, liquid ^4He (boiling point 4.2K at 1 atm) can be used to achieve temperatures down to 1.2K, while pumping on liquid ^3He (boiling point 3.19K at 1 atm) can be used to go down to $\sim 250\text{mK}$ owing to the higher vapor pressure of ^3He . Reaching temperatures as low as $\sim 10\text{mK}$ requires the so-called “dilution process.”

^4He obeys Bosonic statistics and undergoes a transition to superfluid state at 2.17K, whereas ^3He obeys Fermi statistics. Below 870mK, the ^3He - ^4He mixture undergoes a phase separation into a pure liquid ^3He phase and a dilute phase of ^3He in superfluid ^4He . The working of dilution refrigerators relies on the finite solubility of ^3He in superfluid ^4He down to 0K due to the higher Van der Waals attraction between ^3He - ^4He than ^3He - ^3He . If ^3He atoms are removed from the diluted phase [fig 6.1], ^3He atoms from the concentrated phase cross the phase boundary to occupy the vacant energy states, absorbing energy, thus, providing the cooling at the Mixing Chamber (MXC).

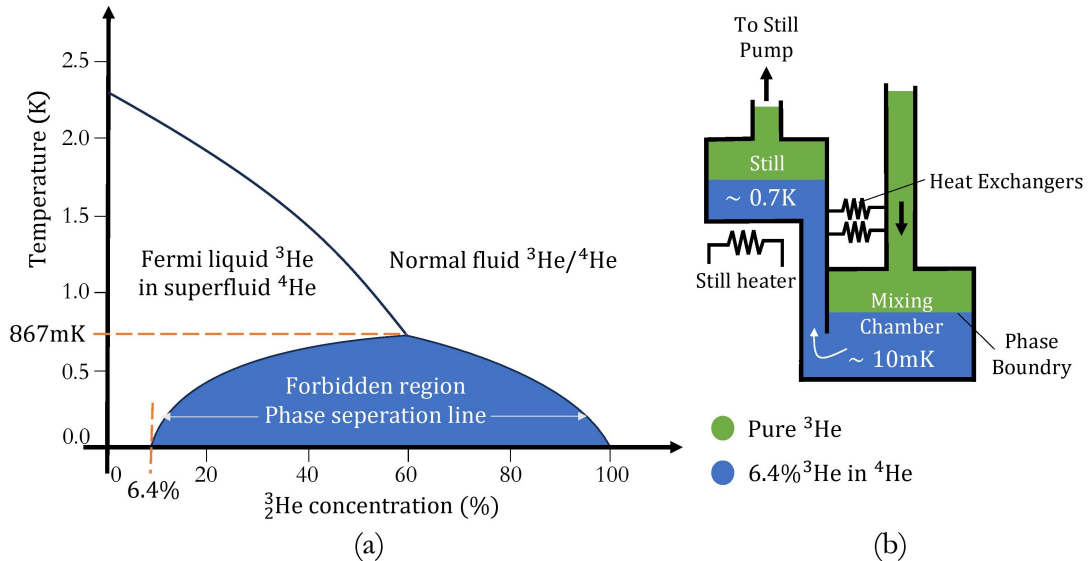


Figure 6.1: (a) Phase diagram for ^3He - ^4He mixing. (b) Schematic showing the key sections of a dilution refrigerator.

The constant ^3He vaporization to the gaseous phase takes place at the Still chamber where external pumping and heating maintain a sufficient rate of vaporization of ^3He , thus sustaining the dilution cycle. ^4He has much lower vapor pressure compared to ^3He at the Still temperature, which is key for selectively maintaining a constant flow of ^3He across the phase boundary at the MXC. Thus, the resulting cooling power at MXC is the flow rate (\dot{n}) multiplied by the associated enthalpy difference due to dilution (ΔH): $\dot{Q} = \dot{n}\Delta H \propto \dot{n}T^2$. Modern dry dilution refrigerators (DRs) use a pulse tube refrigerator (PTR) to pre-cool the DR to about $3K$. It contains an intermediate Joule-Thomson stage, where ^3He passes through a high impedance constriction, which cools it enough to liquify the ^3He on its way to the dilution unit (DU). The ^3He is cooled further before entering the MXC by a series of heat exchangers that thermalize it with various stages ^3He between the Still and the MXC [fig 6.1].

Setup

Observing the discretization of energy states of electrons confined in a quantum dot requires thermal excitations to be suppressed. Particularly, to be able to exploit the Zeeman split electron spin states as a two-level quantum system, the thermal energy $k_B T$ must be smaller than the splitting $g\mu_B B$ which is of the order of the order of a hundred μV (in Si at 1T). This requires cooling the device down to cryogenic temperatures. The experiments were conducted in a Bluefors LD400 dry dilution refrigerator

(DR) equipped with a 9T NbTi superconducting magnet.

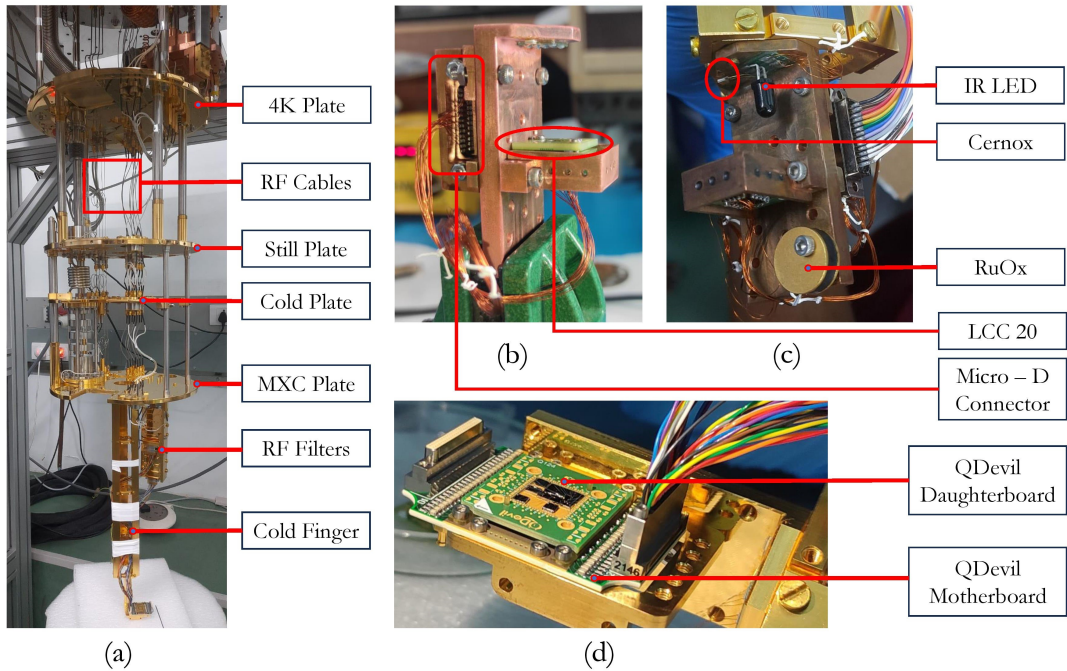


Figure 6.2: (a) Bluefors LD400. (b), (c) Images of the in-house DC sample holder with an LCC-20 chip carrier, IR LED, and RuOx and Cernox temperature sensors. (d) QDevil PCB (motherboard + daughterboard) for RF and DC measurements.

The DR consists of consecutive stages, with each at a lower temperature than the one above during operation, with the MXC being the last plate, reaching temperatures down to 10mK. Initially, the 4K, Still, and MXC plates are thermalized using heat switches. This is when the 4K plate is thermalized to the pulse tube (PT), which provides the cooling power to pre-cool the system to low enough temperatures to start the dilution cycle. This also cools the NbTi magnet down to $\sim 3.9\text{K}$. Upon reaching temperatures low enough to start the dilution process, the heat switches are “turned off” (exchange gas in the chambers is absorbed by cooling down charcoal traps). This thermally isolates the plates below 4K, which are cooled to lower temperatures when the ^3He - ^4He is circulated. The Still chamber is heated and is pumped on by a molecular turbo pump backed by a scroll pump to sustain the ^3He flow. The 4K, Still plate, Cold plate, and the MXC plate are typically at $3.5 - 4\text{K}$, $\sim 800\text{mK}$, 500mK , and 10nK .

The sample is mounted on a cold finger suspended on the MXC plate. The significant thermal mass of the cold finger and RF filter setup means that the temperature of

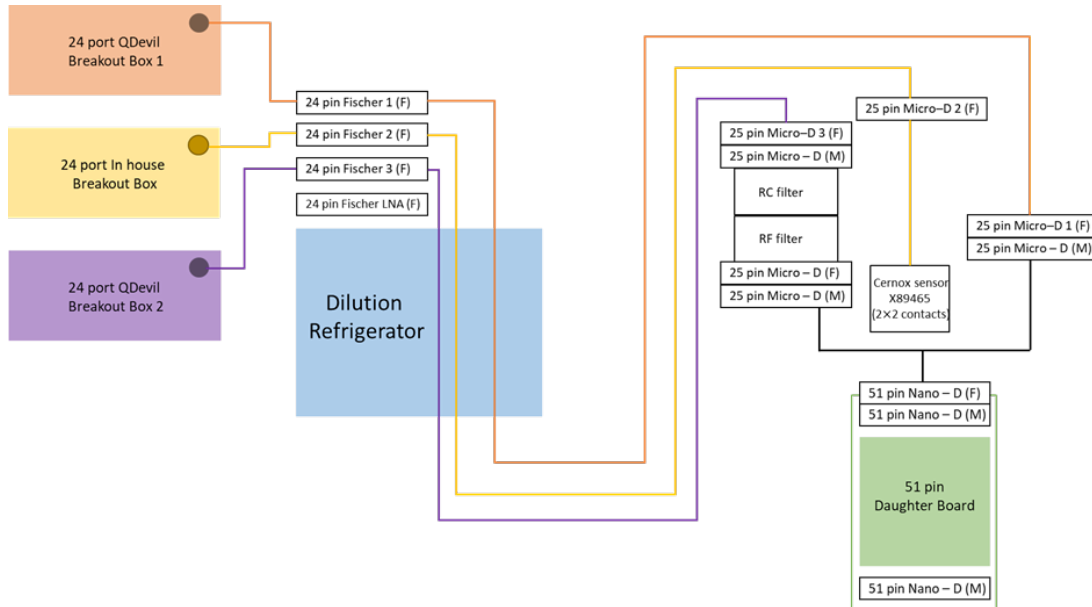


Figure 6.3: Schematic of wiring of the DC lines in the DR along with in-house wiring for temperature sensors.

the sample mounted at the bottom of the cold finger differs slightly from the MXC temperature, thus requiring dedicated sensors mounted close to the sample holder for certain temperature-dependent measurements. The sample temperature at the bottom of the cold finger is monitored using a combination of LakeShore Cernox [1.40K to 325K] and Ruthenium Oxide - RuO_x [42mK to 45K] sensors. Lock-in measurement of the resistance allows for the precise real-time monitoring of sample temperature, which is fully automated, with dynamic sensitivity and excitation voltage, using a QCoDeS-based driver to avoid self-heating of the sensor resistor. Measurements were done with the sample mounted on the QDevil PCB for RF + DC measurements and, alternatively, an in-house sample holder with an LCC-20 chip carrier for DC and low-frequency lock-in measurements. The RuO_x and Cernox sensors and an Infrared LED are mounted at the bottom of the cold finger as shown in [fig 6.2]. The infrared LED is effective in increasing the carrier density in the 2DEG, consequently increasing the quality of contact with the 2DEG at base temperature in the case of GaAs|AlGaAs heterostructures. This is because the carriers in the quantum well are donated by the modulation-doped Si layer, which can get trapped in specific defect sites - DX centers. IR excitation allows these charges to cross the barrier at the heterostructure interface [fig 2.1 (b)] entering the quantum well.

For low frequency or DC measurements, the QDevil motherboard PCB is equipped with 48 lines connected to bonding pads through the daughterboard [fig 6.3]. These lines have low-pass filters to filter out RF noise. 16 RF lines from mini-coax connectors are coupled capacitively through bias tees to combine with DC bias from 16 out of the 48 DC lines. These are intended for the fast gates of the QD device. The daughterboard has four high-frequency lines capable of carrying signals up to 12GHz, specifically for resonator circuits or reflectometry.

6.2 Reflectometry

Fast charge sensing by measuring the damping of a 1.7GHz resonant circuit was suggested by R. J. Schoelkopf et al. [16]. This allowed for high operation frequencies., much above the frequency regime where $1/f$ charge noise is prominent. The basic principle of reflectometry is the partial reflection of an AC signal in a transmission line due to impedance mismatch with the 50Ω transmission line impedance. This impedance, in turn, depends on the SET resistance. Most importantly, the apparatus is designed such that one can operate in the regime where the signal reflection is most sensitive to any impedance changes of the charge sensor SET.

The reflection coefficient for a signal of frequency ω labelled $\Gamma(\omega)$, for a transmission line with impedance Z_0 terminated by an impedance $Z = Z(\omega)$ is:

$$\Gamma(\omega) = \frac{Z(\omega) - Z_0}{Z(\omega) + Z_0} \quad (6.1)$$

The reflected power $|\Gamma|^2$ is then a direct measure of Z . An indicator with impedance $X_L = R_L + i\omega L$ is used to form an LC circuit with the parasitic capacitance (C_p) of the line and the device (SET) capacitance. The components are chosen to allow for a sharp response of the circuit to change in sample impedance (R_D) at a fixed resonance frequency f_{res} of the order of 100MHz [fig 6.4]. The total impedance of the circuit is:

$$\begin{aligned} Z(\omega) &= R_L + i\omega L + \frac{R_D}{1 + i\omega C_p R_D} \\ &= R_L + \frac{R_D}{1 + \omega^2 C_p^2 R_D^2} + i \left(\omega L - \frac{\omega C_p R_D^2}{1 + \omega^2 C_p^2 R_D^2} \right) \\ &\simeq R_L + \frac{R_D}{\omega^2 C_p^2 R_D^2} + i \left(\omega L - \frac{1}{\omega C_p} \right) \end{aligned} \quad (6.2)$$

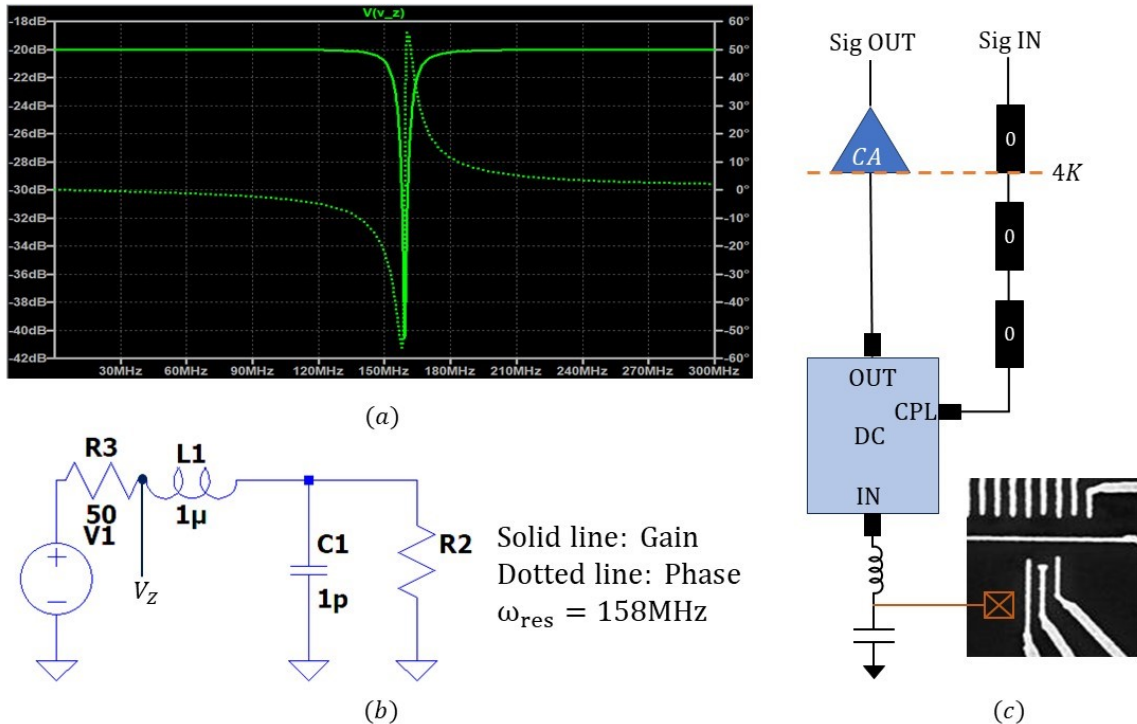


Figure 6.4: (a) AC power at V_Z for different signal frequencies. A sharp dip reflected power $\sim |\Gamma|^2$ is seen at a resonance frequency $\omega_{res} = 158MHz$ (b) The reflectometry circuit equivalent. (c) Circuit to be set up in the dilution refrigerator. CA: cryo-amplifier to amplify reflected signal. DC: directional coupler for selectively sending input signal to the sample and reflected output signal independently in respective RF lines.

$\omega C_p R_D \gg 1$ since typically $\omega \sim 2\pi 100MHz$, $C_p \sim 1pF$, and $R_D \sim 100k\Omega$ (for a typical SET tuned to a few electron regime). At ω_{res} , we need the imaginary part to be 0 for the best possible impedance matching; thus, $\omega_{res} = \sqrt{LC_p}$. This gives $Z(\omega_{res}) \lesssim 20\Omega$ (for $L = \mu H$ and other parameters as stated above), which indeed lies in the regime where Γ is highly sensitive to changes in Z .

The exact frequency ω_{res} is not important for charge sensing and is determined using a vector network analyzer (VNA) to do a frequency sweep and measure dip(s) in S_{11} . Rather, the value of the inductor L is chosen such that given the knowledge of the approximate SET resistance and the parasitic capacitance, the resonance frequency lies in the range where it is within the bandwidth of the cryo-amplifier, attenuation along the RF lines is minimal, and $1/f$ noise is negligible among other considerations

like instrumentation necessary.

IQ modulation or high-frequency Lock-in techniques can be used to measure the phase and amplitude of the signal in reflectometry.¹

¹We will soon be setting up the reflectometry circuit. A more detailed analysis of the same will be a part of BTP-2.

Chapter 7

Future Work and Summary

A recent cool-down of the GaAs|AlGaAs quantum dot device revealed issues with the Ohmics freezing out at base temperature. This is in contrast to the tests done on the same heterostructure without mesa etching, where highly conducting ohmic contacts were measured. The issue has been resolved by modifying the metallization area over the ohmic pockets and modifying the annealing parameters for the contact formation. Thus, the immediate measurement plan for the second part of the BTP remains the measurement and characterization of the quantum dot device in GaAs, primarily dot tuning, Coulomb spectroscopy, and T_1 measurement. In the process, we wish to set up the reflectometry circuit for charge sensing, which will form a critical part when qubit operations or elaborate dot tuning needs to be done.

Certain measurements on the SiGe Hall bar could be done in order to develop a proper understanding of the unexpected mixing of the Hall and SdH signatures. Further, this could be an opportunity to study the valley splitting in the case of the Si quantum well. With key bottlenecks in the fabrication process, namely, the fine gates and implantation for Ohmics already tackled, transport measurements and subsequently qubits in Si remain the main objective.

Appendix A

Appendix

A.1 Quantum Hall Effect

This section is intended as a brief review primarily based on [18] of the theory behind the formulae applied to analyze experimental data in section 2.2.

Using the Drude model of electron transport, we can understand the origin of the transverse Hall voltage (V_H) in the presence of a perpendicular magnetic field. In presence of an out of plane magnetic field $\vec{B} = B\hat{z}$ and an electric $\vec{E} = E_x\hat{x} + E_y\hat{y}$ force on a charge carrier is given by:

$$\vec{F} = \vec{F}_{scat} + \vec{F}_{ext} = \frac{d\vec{p}}{dt}\Big|_{scat} + \frac{d\vec{p}}{dt}\Big|_{ext} \quad (\text{A.1})$$

The relaxation due to scattering is taken into account by incorporating a purely phenomenological constant τ . τ can be thought of as the rate at which a particle loses its momentum completely due to collision events, i.e., $\frac{d\vec{p}}{dt}\Big|_{scat} = -\frac{\vec{p}}{\tau}$. The external force $\vec{F}_{ext} = -e(\vec{E} + \vec{v} \times \vec{B})$ is the Lorentz force. The current density $\vec{j} = -en\vec{v}$. In steady state, $\vec{F} = 0$. This gives:

$$-e(E_x\hat{x} + E_y\hat{y}) = \frac{m}{\tau}(v_x\hat{x} + v_y\hat{y}) + eB(v_x\hat{y} - v_y\hat{x})$$

$$\begin{bmatrix} E_x \\ E_y \end{bmatrix} = \frac{m^*}{e^2 n \tau} \begin{bmatrix} 1 & -\omega_c \tau \\ \omega_c \tau & 1 \end{bmatrix} \begin{bmatrix} j_x \\ j_y \end{bmatrix} \quad (\text{A.2})$$

Here, $\omega_c = \frac{B}{m^* e}$ is the cyclotron frequency. m^* is the effective mass of the electron in the material. Since $\vec{E} = \vec{\rho} \leftrightarrow \vec{j}$, the longitudinal resistivity is a constant ($\rho_{xx} = \rho_{yy} = \sigma_D^{-1}$) whereas the transverse component is linearly dependent on magnetic field

$(\rho_{xy} = -\rho_{yx} = -\sigma_D^{-1} \frac{eB}{m^*})$. Here $\sigma_D = ne^2\tau/m^*$ is the Drude conductivity. For the configuration in figure (3.1), for weak magnetic field ($\omega_c\tau \ll 1$), in steady state, $j_y = 0$, and the fields E_x and E_y are assumed uniform. In that case, the measured voltages are $V_{xx} = E_x L$ and $V_{yx} = E_y W$. The current supplied I is known, thus, $j_x = \frac{I}{W}$.

$$\rho_{xx} = \frac{1}{\sigma_D} = \frac{V_{xx}W}{IL} \quad (\text{A.3})$$

$$\rho_{yx} = \frac{1}{\sigma_D} \frac{eB\tau}{m^*} = \frac{V_{yx}W}{IL} \quad (\text{A.4})$$

Knowing resistivity allows for calculating the carrier density n from the slope of the plot of ρ_{yx} vs B . The mobility can also be calculated as $\mu = |v_d/E_x|$: the ratio of the drift velocity to the electric field. The Hall voltage $V_{xy} = V_H$ is linearly dependent on B , whereas V_{xx} is a constant. This result only holds for low magnetic fields but hints at an essential property of the Hall effect. The Hall voltage is independent of the geometrical parameters L and W . Thus, if one were to make holes (somehow remove carriers) along the bulk of the channel, effectively changing w and L the longitudinal resistance would change, but the Hall voltage would remain unaffected.

The quantum mechanical treatment of the Hamiltonian of the system is needed to understand the features observed experimentally at high magnetic fields. The Hamiltonian in presence of a magnetic field $B\hat{z} = \vec{\nabla} \times \vec{A}$ is:

$$\hat{H} = \frac{1}{2m^*}(\vec{p} + e\vec{A})^2 = \frac{1}{2m^*}((p_x - eBy)^2 + p_y^2) \quad (\text{A.5})$$

Working in the Landau Gauge where $\vec{A} = (-By, 0, 0)$. Here, $[p_x, \hat{H}] = 0$, which implies translational invariance along the y direction, thus motivating the ansatz $\psi(x, y) = e^{ikx}\phi_k(y)$.

$$\hat{H}\psi_k(x, y) = \frac{1}{2m^*}[p_y^2 + (\hbar k - eBy)^2]\psi_k(x, y) = \hat{H}_k\psi_k(x, y) \quad (\text{A.6})$$

$$\hat{H}_k = \frac{1}{2m^*}p_y^2 + \frac{m\omega_c^2}{2}(y - kl_B^2)^2 \quad (\text{A.7})$$

Here, \hat{H}_k is the Hamiltonian of a simple harmonic oscillator displaced along the y -axis by kl_B^2 , where l_B is the magnetic length scale given by:

$$l_B = \sqrt{\frac{\hbar}{eB}} \quad (\text{A.8})$$

The energy eigenvalues and eigenfunctions are:

$$E_q = \hbar\omega_c \left(q + \frac{1}{2} \right) \quad (\text{A.9})$$

$$\tilde{\psi}_{q,k}(x, y) \sim e^{ikx} H_q(y - kl_B^2) e^{-(y - kl_B^2)^2 / 2l_B^2} \quad (\text{A.10})$$

H_q are Hermite polynomial eigenfunctions of the harmonic potential with $q \in \mathbb{N}$ and $k \in \mathbb{R}$. The energy levels depend only on q . Thus, the k values attainable contribute to the degeneracy of these states. The dimensions of the Hall bar are finite along the x and y directions, L and W , respectively. The momentum k is quantized in units of $2\pi/L$. Since $0 \leq y \leq W$, we expect $0 \leq k \leq W/l_B^2$ for the state to be localized around $y = kl_B^2$. Thus, the number of states is:

$$N(B) = \frac{L}{2\pi} \int_0^{W/l_B^2} dk = \frac{eBA}{2\pi\hbar} = \frac{AB}{\Phi_0} \quad (\text{A.11})$$

Here, $A = LW$ is the area, and the quantum of magnetic flux is defined as $\Phi_0 = \frac{2\pi\hbar}{e}$. The degeneracy of each Landau level is macroscopic. If the spin splitting is negligible, for carrier density n , nA electrons must be distributed between available Landau levels. Thus, the number of occupied Landau levels, also called the filling factor, is given by (labeled ν):

$$\nu = \frac{nA}{N} = \frac{nh}{eB} \quad (\text{A.12})$$

In the presence of an electric field $E\hat{y}$ in the y direction (analogous to Hall voltage), a term $\Phi_H = eEy$ must be added to the Hamiltonian. The procedure for solving the problem remains the same as above, just with an added term that acts like a shift of origin along the y -axis. The eigenstates and eigenenergies are now given by:

$$\psi(x, y) = \psi_{q,k}(x, y - mE^2/eB^2) \quad (\text{A.13})$$

$$E_{q,k} = \hbar\omega_c \left(q + \frac{1}{2} \right) - eE \left(kl_B^2 + \frac{eE}{m\omega_c^2} \right) + \frac{mE^2}{2B^2} \quad (\text{A.14})$$

The degeneracy of the Landau levels is now lifted since the energy depends on k . The x direction group velocity $v_x = \frac{1}{\hbar}\partial_k E_{q,k} = -E/B$ is nonzero.

To explain the experimentally observed Hall resistivity plateaus, we compute the current density for particles moving in a magnetic field when ν landau levels are filled (Fermi energy E_F is not overlapping with a Landau level):

$$\begin{aligned} \vec{J} &= -\frac{e}{mA} \sum_{\text{states}} \langle \psi | -i\hbar\vec{\nabla} + e\vec{A} | \psi \rangle \\ &= -\frac{e}{mA} \sum_{q=1}^{\nu} \sum_k \langle \psi_{q,k} | -i\hbar\vec{\nabla} + e\vec{A} | \psi_{q,k} \rangle \end{aligned} \quad (\text{A.15})$$

$$J_y = -\frac{e}{mA} \sum_{q=1}^{\nu} \sum_k \langle \psi_{q,k} | -i\hbar\partial_y | \psi_{q,k} \rangle = 0 \quad (\text{A.16})$$

Here, $\psi_{q,k}$ are the eigenstates obtained in equation A.10. The momentum expectation for harmonic oscillator states is zero.

$$\begin{aligned} J_x &= -\frac{e}{mA} \sum_{q=1}^{\nu} \sum_k \langle \psi_{q,k} | -i\hbar\partial_x - eBy | \psi_{q,k} \rangle \\ &= -\frac{e}{mA} \sum_{q=1}^{\nu} \sum_k \langle \psi_{q,k} | \hbar k - eBy | \psi_{q,k} \rangle = e\nu \sum_k \frac{E}{AB} \end{aligned} \quad (\text{A.17})$$

Since $\langle \psi_{q,k} | y | \psi_{q,k} \rangle = \hbar k / eB + mE / eB^2$ due to the effective origin shift. For $\vec{E} = E\hat{y}$ we get $\vec{J} = e\nu E / \Phi_0 \hat{x} = \vec{\sigma} \cdot \vec{E}$. This gives:

$$\sigma_{xx} = 0, \quad \sigma_{xy} = \frac{e\nu}{\Phi_0} \Rightarrow \rho_{xx} = 0, \quad \rho_{xy} = \frac{\Phi_0}{e\nu} = \frac{h}{e^2} \frac{1}{\nu} \quad (\text{A.18})$$

So far, we have ignored electron spin and disorders in the system. Spin splitting splits each Landau level into two, separated by $g\mu_B B$. Disorders are perturbations to the system that break the degeneracy of each Landau level. This leads to the broadening of each Landau level, forming bands. Disorders also lead to the localization of states around the disorder potential's extrema. These states are “stuck” to closed orbits around these extrema. Thus, extended states that move throughout the sample are guaranteed only at the edges along the equipotential contours (which are sparse in the bulk). Here, the underlying assumption is that the disorder potential V is much smaller than the landau level separation ($V \ll \hbar\omega_c$), and it varies only over length scales much larger than the magnetic length ($|\vec{\nabla}V|l_B \ll \hbar\omega_c$).

Conduction through these edge modes is key to the robustness of the Hall effect against disorders. Classically, in the presence of a strong magnetic field, electrons tend to follow “skipping orbits” along the two edges. The motion of the electrons along each edge is restricted in one direction, with the two edges having opposite chirality. In the absence of an electric field, the net current is zero. To understand the features of the ρ_{xx} and ρ_{yx} curves, consider a rectangular sample geometry finite along the y-axis (width W). The Hamiltonian then looks like:

$$\hat{H} = \frac{1}{2m^*} ((p_x - eBy)^2 + p_y^2) + V(y) \quad (\text{A.19})$$

The eigenstates $\psi_{n,k}$ (eq A.10) are localized in the y direction on length scales of l_B around $x_0 = kl_B^2$, and thus for a smooth potential $V(y)$ effectively acts like an added

$\Phi = V(y_0) + \frac{\partial V}{\partial y}(y - y_0)$ term to the Hamiltonian. As seen previously (eq A.13), this just leads to a drift velocity along the x direction:

$$v_x = -\frac{1}{eB} \frac{\partial V}{\partial y} \quad (\text{A.20})$$

The drift is along $+x$ along one edge and $-x$ along the other. These are the so-called “skipping orbits”.

As discussed above, when the Fermi energy doesn't overlap with a Landau level, the conduction occurs via edge modes. On the contrary, when a broadened Landau level is partly filled (Fermi energy E_F lies within the Landau level), the electrons in the bulk can participate in conduction, leading to increased scattering and, thus, larger resistance. These jumps in resistance occur when the Fermi energy overlaps with a Landau level, which in turn depends on the magnetic field. When a Landau level is half-filled ($\nu = m/2 = nh/eB$ where $m \in \mathbb{N}$), a maximum in longitudinal resistance is seen. ρ_{xx} is periodic in $1/B$, allowing the calculation of number density as:

$$n = \frac{e}{h} \left(\frac{1}{\frac{1}{B_i} - \frac{1}{B_{i+1}}} \right) \quad (\text{A.21})$$

Bibliography

- [1] B. L. Booth and A. W. Ewald. Spin splitting of landau levels and the effective g factor in gray tin. *Phys. Rev.*, 186:770–774, Oct 1969.
- [2] Supriyo Datta. *Quantum Transport: Atom to Transistor*. Cambridge University Press, 2005.
- [3] David P. DiVincenzo. The physical implementation of quantum computation. *Fortschritte der Physik*, 48(9-11):771–783, sep 2000.
- [4] J. M. Elzerman, R. Hanson, L. H. Willems van Beveren, B. Witkamp, L. M. K. Vandersypen, and L. P. Kouwenhoven. Single-shot read-out of an individual electron spin in a quantum dot. *Nature*, 430(6998):431–435, jul 2004.
- [5] R. Hanson, L. P. Kouwenhoven, J. R. Petta, S. Tarucha, and L. M. K. Vandersypen. Spins in few-electron quantum dots. *Reviews of Modern Physics*, 79(4):1217–1265, oct 2007.
- [6] Manus Hayne, A USHER, J J HARRIS, and C T FOXON. Exchange enhancement of the landau-level separation for two-dimensional electrons in gaas/galxas heterojunctions. *Physical review B*, 46(15):9515–9519, October 1992. © 1992 The American Physical Society.
- [7] A Isihara and L Smrcka. Density and magnetic field dependences of the conductivity of two-dimensional electron systems. *Journal of Physics C: Solid State Physics*, 19(34):6777, dec 1986.
- [8] K. v. Klitzing, G. Dorda, and M. Pepper. New method for high-accuracy determination of the fine-structure constant based on quantized hall resistance. *Phys. Rev. Lett.*, 45:494–497, Aug 1980.

- [9] Leo P. Kouwenhoven, Charles M. Marcus, Paul L. McEuen, Seigo Tarucha, Robert M. Westervelt, and Ned S. Wingreen. *Electron Transport in Quantum Dots*, pages 105–214. Springer Netherlands, Dordrecht, 1997.
- [10] N. S. Lai, W. H. Lim, C. H. Yang, F. A. Zwanenburg, W. A. Coish, F. Qassemi, A. Morello, and A. S. Dzurak. Pauli spin blockade in a highly tunable silicon double quantum dot. *Scientific Reports*, 1(1), oct 2011.
- [11] Daniel Loss and David P. DiVincenzo. Quantum computation with quantum dots. *Phys. Rev. A*, 57:120–126, Jan 1998.
- [12] D. Maradan, L. Casparis, T.-M. Liu, D. E. F. Biesinger, C. P. Scheller, D. M. Zumbühl, J. D. Zimmerman, and A. C. Gossard. GaAs quantum dot thermometry using direct transport and charge sensing. *Journal of Low Temperature Physics*, 175(5-6):784–798, apr 2014.
- [13] X. Mi, J. V. Cady, D. M. Zajac, P. W. Deelman, and J. R. Petta. Strong coupling of a single electron in silicon to a microwave photon. *Science*, 355(6321):156–158, jan 2017.
- [14] Michael A. Nielsen and Isaac L. Chuang. *Quantum Computation and Quantum Information: 10th Anniversary Edition*. Cambridge University Press, 2010.
- [15] John Preskill. Lecture notes for physics 229: Quantum information and computation, 1998.
- [16] R. J. Schoelkopf, P. Wahlgren, A. A. Kozhevnikov, P. Delsing, and D. E. Prober. The radio-frequency single-electron transistor (rf-set): A fast and ultrasensitive electrometer. *Science*, 280(5367):1238–1242, 1998.
- [17] C. B. Simmons, J. R. Prance, B. J. Van Bael, Teck Seng Koh, Zhan Shi, D. E. Savage, M. G. Lagally, R. Joynt, Mark Friesen, S. N. Coppersmith, and M. A. Eriksson. Tunable spin loading and T_1 of a silicon spin qubit measured by single-shot readout. *Phys. Rev. Lett.*, 106:156804, Apr 2011.
- [18] David Tong. Lectures on the quantum hall effect, 2016.
- [19] C. Volk, A. Zwerver, Uditendu Mukhopadhyay, Pieter Eendebak, C. Diepen, Juan Pablo Dehollain, T. Hensgens, T. Fujita, Christian Reichl, W. Wegschei-

- der, and L. Vandersypen. Loading a quantum-dot based “qubyte” register. *npj Quantum Information*, 5, 12 2019.
- [20] Jun Yoneda, Tomohiro Otsuka, Tatsuki Takakura, Michel Pioro-Ladrière, Roland Brunner, Hong Lu, Takashi Nakajima, Toshiaki Obata, Akito Noiri, Christopher J. Palmstrøm, Arthur C. Gossard, and Seigo Tarucha. Robust micromagnet design for fast electrical manipulations of single spins in quantum dots. *Applied Physics Express*, 8(8):084401, jul 2015.
- [21] D. M. Zajac, A. J. Sigillito, M. Russ, F. Borjans, J. M. Taylor, G. Burkard, and J. R. Petta. Resonantly driven CNOT gate for electron spins. *Science*, 359(6374):439–442, jan 2018.

This is the initial draft of the BTP-I report to be submitted on 06-11-23. Further sections on Pauli spin blockade and quantum dot characterization will be added without any modification to the overall flow of the content. The final draft will be shared well before the presentation with the examiners.